

Low-frequency current variability observed at the shelfbreak in the northeastern Gulf of Mexico: November 2004–May 2005

M.R. Carnes, W.J. Teague*, E. Jarosz

Naval Research Laboratory, Stennis Space Center, MS 39529-5004, USA

Received 5 June 2007; received in revised form 25 September 2007; accepted 8 October 2007

Available online 22 October 2007

Abstract

Fourteen acoustic Doppler current profilers (ADCPs) were deployed on the shelf and slope for 1 year just west of the DeSoto Canyon in the Northeastern Gulf of Mexico by the Naval Research Laboratory (NRL) as part of its Slope to Shelf Energetics and Exchange Dynamics (SEED) project. The winter and spring observations are discussed here in regards to the low-frequency current variability and its relation to wind and eddy forcing. Empirical orthogonal function (EOF) analyses showed that two modes described most of the current variability. Wind-forced variability of the along-shelf flow was the main contributor in Mode 1 while eddies contributed much of the variability in Mode 2. Wind-stress controlled currents on the shelf and slope at time scales of about a week. On longer time scales, variations in the currents on both the outer shelf and slope appear to be related to seasonal variations in the time-cumulated wind stress curl. Winds were dominant in driving the along-shelf transports, particularly along the slope. However, the effective wind stress component was found to be aligned with the west Florida shelf direction rather than the local shelf direction. Eddy intrusions, which were more numerous in winter and spring than in summer and fall, and winds were found to contribute significantly to cross-shelf exchange processes.

Published by Elsevier Ltd.

Keywords: Coastal current; Continental shelf; Continental slope; Wind stress curl; Northeastern Gulf of Mexico; (28–31N; 86–90W); ADCP moorings; Slope circulation

1. Introduction

Characterizing the flow near the outer edges of the continental shelf and the upper slope is important for determining the exchange mechanisms between the shelf and deep water. It is known that the circulation in the western Gulf of Mexico is driven by both wind stress curl (Sturges and Blaha, 1976; Blaha and Sturges, 1981) and detached rings from the Loop Current. Using ship drift data, Sturges (1993) showed an annual cycle in the western boundary current that is strongest in July and weakest in October. He suggested that the annual variation is driven by the annual variation in wind stress curl augmented by Ekman pumping over the western gulf. The role of rings in the annual cycle can be argued to be small since several studies have shown that rings shed from the Loop current

do not have significant annual periodicity (Vukovich, 1988; Sturges, 1992; Maul and Vukovich, 1993).

Currents near the shelf edge in the northeastern Gulf of Mexico are also thought to be driven by wind and mesoscale eddies, in addition to buoyancy-driven coastal circulations. These processes are likely to be intermixed. This region is different from the western gulf because it is rarely directly influenced by Loop Current rings, or by the Loop Current extension (Vukovich et al., 1979; Huh et al., 1981; Wiseman and Dinnel, 1988). However, satellite imagery has revealed complex eddy-like structures in this region that are associated with frontal eddies that travel around the periphery of the Loop Current and Loop Current eddies (Vukovich and Maul, 1985). In addition, the DeSoto Canyon is believed to generate eddies by the interaction of strong along-shelf currents with the sharp bends in canyon topography (Weisberg et al., 2005). The dominant forcing mechanisms of the currents are not known although there have been numerous studies (Blaha

*Corresponding author. Tel.: +1 228 688 4734; fax: +1 228 688 5997.

E-mail address: teague@nrlssc.navy.mil (W.J. Teague).

and Sturges, 1981; Hamilton and Lee, 2005; Biggs et al., 2005; Morey et al., 2005).

The zonal components of the currents and winds, in the northeastern gulf west of 85°W, were found to be highly coherent on a seasonal time scale (Hsueh and Weisberg, 2002). Model studies have focused on direct wind forcing in the absence of the Loop Current and Loop Current rings (Li and Weisberg, 1999; Yuan, 2002). Using data from satellites and current meters in conjunction with a model, Wang et al. (2003) presented evidence for eddy-induced shelfbreak and slope circulation in the northeastern gulf. Monthly means and movies provided from drifter observations have shown that the near-surface currents on the shelf consist primarily of motions that are back-and-forth zonally (Johnson, 2005). Mean flows averaged over many weeks are small when compared with the daily currents. Flow reversals are believed to be caused by local winds and eddy intrusions. The shelf edge and slope, together, have proven to be difficult regions to understand and for a single model to portray. Forcing mechanisms including both coastal and deep ocean processes, and poorly resolved shelf-break topography contribute to the problem. Modeling efforts such as the Hybrid Coordinate Ocean Model (HYCOM) (Chassignet et al., 2007) are being developed to address these problems.

The Naval Research Laboratory has conducted an intensive measurement program of the outer continental shelf and upper slope waters off the Gulf Coast as part of its Slope to Shelf Energetics and Exchange Dynamics (SEED) project (Teague et al., 2006), with the primary focus on current measurements. A major goal of SEED is to understand the physical processes that control the exchange of mass, momentum, heat, and water properties along and across the shelf break. The low-frequency currents, corresponding to periods greater than 40 h, for summer and fall during the first deployment (D1) have been described by Teague et al. (2006). Currents and waves under Hurricane Ivan, which passed directly over the moorings on September 15, 2004, are discussed in Teague et al. (2007). Topographic Rossby waves are discussed in Hallock et al. (submitted).

The second half of the measurements, for winter and spring during the second deployment (D2), are discussed in this paper in regards to the low-frequency current variability and its relation to wind and eddy forcing. We address the dominant forcing mechanisms and try to separate the eddy contributions from the wind-induced background flow. This paper combined with Teague et al. (2006) also sets the stage for focused studies on specific dynamical processes prompted by these analyses. The data are described in Section 2, some basic statistics are given in Section 3, general current flow is discussed in Section 4, and barotropic flow is described in Section 5. Empirical orthogonal functions (EOFs) are analyzed in Section 6. The relationship of the currents with the winds is examined in Section 7. Eddy observations and impact on the currents are discussed in Section 8 and seasonal variability is

discussed in Section 9. Finally, summary and conclusions are given in Section 10.

2. Data

Fourteen ADCP moorings were deployed in May 2004 for a year in the northeastern Gulf of Mexico on the outer continental shelf and upper slope just west of the DeSoto Canyon at water depths ranging between 60 and 1000 m (Fig. 1). The average horizontal spacing between instruments was about 15 km. All of the moorings were recovered in November 2004 and 13 were redeployed at the same locations (M14 was not redeployed due to equipment failure). Final recovery of the moorings was accomplished in May 2005. The May–November 2004 data (D1) were reported on by Teague et al. (2006). Table 1 provides positions, times, instrument depths, bottom depths, velocity bin levels, and instrument types for the deployment from November 2004 to May 2005 (D2). Days refer to decimal day of the year where day 0 corresponds to January 1, 2004.

Six moorings were deployed on the outer shelf in two lines consisting of three moorings each at depths of 60 m (M1–M3, Line 1 (L1)) and 90 m (M4–M6, Line 2 (L2)) (Fig. 1). They were deployed in Trawl-Resistant Bottom Mounts (TRBMs) which utilized dome-shaped mounting pods known as Barnys after their barnacle-like shape (Perkins et al., 2000). The Barny mounts were equipped with RD Instruments Workhorse ADCPs operating at 300 kHz and Sea-Bird Electronics wave/tide gauges. The ADCP heads were situated about 0.5 m off the bottom and recorded current profiles from near the bottom to near the surface with 2 m vertical resolution every 15 min with an accuracy of $0.5\% \pm 0.5$ cm/s. The random error which is dependent on the depth-bin size and number of pings per sampling interval is reported as a standard deviation of 1.34 cm/s. At the moorings, near-bottom pressure and temperature were also measured.

Seven moorings were deployed down the continental slope in two lines consisting of four moorings at depths of 500 m (M7–M10, Line 3 (L3)) and three moorings at depths of 1000 m (M11–M13, Line 4 (L4)) (Fig. 1). These moorings consisted of RD Instruments Long Ranger ADCPs operating at 75 kHz contained in 45-in diameter Flotation Technology buoys. Current profiles of approximately 500 m in vertical extent were measured every hour with 10 m resolution at an accuracy of $1\% \pm 0.5$ cm/s. The random error is reported as a standard deviation of 1.30 cm/s. The moorings near 500 m depth were deployed 10 m from the bottom and recorded near-full water column current profiles. The moorings near 1000 m depth were located about 500 m above the bottom and hence only measured the upper water column. At these moorings, pressure and temperature at the depth of the ADCP were also measured. Additionally, for the three 1000 m moorings, Aanderaa RCM9 Doppler current meters were located at about 900 m depth and recorded current speed,

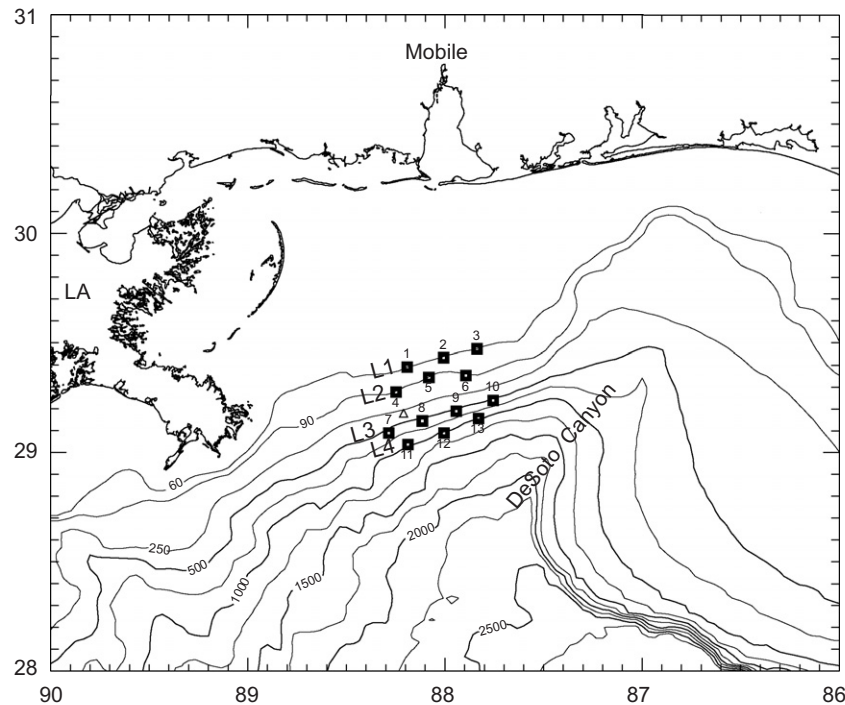


Fig. 1. SEED moorings (squares) and bathymetry (m) are shown for lines L1–L4. NDBC buoy 42040 is indicated by the triangle.

Table 1
Mooring summary

M	LAT	LON	Start day	End day	dt	z1	zn	dz	Bottom	Type
			2004	2005						
1	29.39	−88.19	311	122	.25	6	56	2	60	TRBM
2	29.43	−88.01	311	122	.25	5	57	2	60	TRBM
3	29.47	−87.84	311	122	.25	6	56	2	60	TRBM
4	29.28	−88.25	311	96	.25	10	82	2	88	TRBM
5	29.34	−88.08	311	122	.25	8	84	2	89	TRBM
6	29.35	−87.89	311	123	.25	8	84	2	87	TRBM
7	29.09	−88.28	317	124	1.0	53	493	10	515	Long Ranger
8	29.14	−88.11	317	124	1.0	48	498	10	518	Long Ranger
9	29.19	−87.94	317	124	1.0	52	492	10	518	Long Ranger
10	29.24	−87.76	317	124	1.0	47	507	10	518	Long Ranger
11	29.04	−88.19	317	123	1.0	48	498	10	1016	Long Ranger
					1.0	912				AA RCM9
12	29.09	−88.00	317	123	1.0	48	498	10	1038	Long Ranger
					1.0	934				AA RCM9
13	29.16	−87.83	317	123	1.0	48	498	10	1025	Long Ranger
					1.0	921				AA RCM9

Columns correspond to mooring number, latitude, longitude, start day and end day, sampling interval in hours (dt), depths (in m) of top velocity bin (z1) and bottom velocity bin (zn), and bin interval (dz); bottom depth in m, and instrument type (TRBM—trawl-resistant bottom mounted 300 kHz ADCP, Long Ranger—75 kHz ADCP, AA RCM9—Aanderra RCM9 acoustic current meter).

current direction, temperature, and pressure. Their velocity accuracy is 0.5 cm/s (standard deviation) or $\pm 1\%$ of actual speed (whichever is greater).

The data return was excellent and did not require any editing. Removal of measurement error and high-frequency motions, not of interest here, was accomplished by applying a sixth-order low-pass Butterworth filter with a 40-h cutoff period. The bathymetric contours within the

mooring array were approximately parallel and were oriented about 20° counterclockwise from the east (Fig. 1). Since currents at the shelf break and along the continental slope in the northern Gulf of Mexico often follow the bathymetry (Teague et al., 2006) the current data were rotated 20° counterclockwise from the east so that u components were along shelf and v components were cross shelf for some of the analyses performed here.

Positive u values are referred to as upcoast and negative u values are referred to as downcoast (the propagation direction of coastal Kelvin waves in the northern hemisphere against a northern shoreline). Positive and negative v values are referred to as onshore and offshore, respectively.

3. Statistics

Statistics for D2, consisting of average along-shelf (\bar{U}) and average cross-shelf (\bar{V}) velocities, and their standard deviations, standard errors, maximum values including maximum speed and direction, integral time scales, mean kinetic energies, and mean eddy kinetic energies are provided in Table 2. In order to conserve table space, statistics for only three to six depth levels are presented but are found to provide a good description of the statistical parameters over depth. Maximum speed (Spd_{max}) is computed from u and v and need not correspond with the individual maximum component velocities in Table 2. Maximum direction (Dir_{max} , in $^{\circ}T$, measured clockwise from the north, 0°) is the direction that corresponds with the maximum speed. The standard error listed here is defined as the standard deviation divided by the square root of the number of degrees of freedom, which is estimated as the sample period divided by the integral time scale. The integral time scale is defined as the discrete integral of the time-lagged autocorrelation function from zero lag to the first zero crossing after demeaning and detrending the time series. Integral time scales ranged from approximately 2 to 30 days during D1 (Teague et al., 2006). During that period, the time scales appeared to be modulated at periods of about a week and several months. This is not the case for D2 (Fig. 2a) where integral time scales ranged from a couple of days to about a week on the shelf and from 1 to 2 weeks on the slope, with the longer time scales occurring in the along-shelf direction. The shorter time scales in D2 result mainly from increased wind stress variability from the passage of cold fronts (discussed in Section 7) and perhaps to increased eddy activity (Section 8).

The maximum speed of 62 cm/s was observed over the slope on L3 at both M9 and M10, but at directions of 93 and 251 $^{\circ}T$ and depths of 52 m (at the top of the measured velocity profile) and 198 m, respectively. Maximum speeds within the profiles on the shelf sometimes occurred well below the measured near surface values. The maximum speed on the shelf, 61 cm/s, was observed at M6 on L2 at 50 m depth, near the middle of the measured velocity profile. Maximum speeds within the profiles on the slope generally decreased with depth, except at M10.

Mean currents were generally upcoast and offshore on the shelf. On the slope, mean flows were usually upcoast in the upper couple of hundred meters but downcoast in the lower part of water column while mean cross-shelf currents were highly variable. At 900 m, mean currents were predominately downcoast. Mean along-shore currents

during D2 were similar to those in D1 (Teague et al., 2006) on the slope but different on the shelf where mean currents were downcoast near the bottom during D1. Mean cross-shelf flows on the shelf were all offshore during D2 while both onshore and offshore flows in the mean were found during D1.

Mean eddy kinetic energy (EKE) on the shelf ranged from a low of about $52 \text{ cm}^2/\text{s}^2$ near the bottom at M5 to a high of $160 \text{ cm}^2/\text{s}^2$ at 50 m depth at M6. Mean EKE on the slope ranged from $13 \text{ cm}^2/\text{s}^2$ at 912 m depth at M11 to $267 \text{ cm}^2/\text{s}^2$ at 48 m depth at M13. Mean kinetic energy (MKE) generally ranged from about 1 to $50 \text{ cm}^2/\text{s}^2$. EKE was dominant due to the weak mean flows. During D2 mean EKE was typically smaller on the shelf than during D1 (Teague et al., 2006), but it was comparable and sometimes larger on the slope.

4. Currents

The SEED region encompassed both the shelf and slope. There were periods when both shelf and slope current variations were clearly connected as well as periods when they were disconnected (Fig. 2). Currents were dominated by the along-shelf components during D2. These components also dominated during D1 (Teague et al., 2006) but at lower frequencies, i.e., on scales of 1–2 months instead of 1–2 weeks found for D2 as evidenced by the integral time scales (Table 2) and visually in Fig. 2. In addition, eddies had more of an impact on the SEED region during D2 (see Section 8) than during D1.

Based primarily on inspection of the along-shelf velocities (Fig. 2a), four time periods (P1–P4) were identified by the contrasting current structures, particularly evident on the slope along L3 and L4. Strong upcoast flows dominated during P1 which ranged from November 6, 2004 to January 22, 2005 (days 310–387, where day 0 corresponds to January 1, 2004) while during P2 (January 22–February 19, 2005 or days 387–415) strong downcoast flows dominated. During P3 (February 19–April 5, 2005 or days 415–460) flow switched to generally upcoast and during P4 (April 5–May 5, 2005 or days 460–490) currents were again downcoast. Flows appeared more variable on the shelf. Several periods of relatively strong onshore and offshore flows occurred on both the shelf and the slope (Fig. 2b) but appeared to be disjointed. The strong onshore and offshore flow events are caused by slope eddies. There are strong eddy interactions with the slope down to about 500 m (M11) and some smaller interactions with the shelf (M5) in the February–March time period. Eddies have strong effects on both the slope down to nearly 200 m (M9 and M13) and the shelf (almost full water column at M6) during the April time period. These slope eddies are further discussed in the Section 8.

The contrasting current structure between the four periods is also revealed in the time-averaged profiles of velocity shown in Fig. 3. Velocity maximums commonly occurred below the near-surface observed velocities. During

Table 2
Basic statistics over D2 for selected depth levels

	<i>Z</i>	\bar{U}	σ_u	S.E. _{<i>u</i>}	<i>U</i> _{min}	<i>U</i> _{max}	\bar{V}	σ_v	S.E. _{<i>v</i>}	<i>V</i> _{min}	<i>V</i> _{max}	<i>Spd</i> _{max}	<i>Dir</i> _{max}	<i>IT</i> _{<i>u</i>}	<i>IT</i> _{<i>v</i>}	<i>MKE</i>	<i>EKE</i>
M1	6	−0.84	9.86	2.33	−33.68	25.31	−2.61	8.71	1.15	−40.77	18.90	41.31	170.30	9.79	3.07	3.76	86.57
M1	30	2.72	8.41	1.89	−21.56	36.87	−3.60	7.75	1.41	−29.18	20.89	36.87	90.53	8.84	5.77	10.18	65.46
M1	50	0.74	7.34	1.13	−23.28	33.43	−3.41	7.39	1.11	−32.62	13.77	33.72	97.59	4.12	3.96	6.09	54.23
M2	5	0.04	10.54	2.13	−31.47	28.43	−2.75	9.36	1.06	−41.68	27.73	41.68	179.65	7.15	2.26	3.79	99.36
M2	31	1.30	10.54	1.79	−26.21	35.02	−1.70	5.74	0.65	−23.92	14.56	36.03	103.59	5.05	2.27	2.29	72.07
M2	51	−0.87	10.85	1.65	−29.69	31.86	−1.62	4.55	0.45	−26.47	9.63	37.80	131.79	4.03	1.74	1.69	69.25
M3	6	1.99	12.58	1.98	−31.04	31.08	−1.57	8.27	0.92	−27.89	17.09	31.68	101.17	4.32	2.16	3.21	113.30
M3	30	3.82	12.92	2.28	−25.15	43.42	−1.10	5.39	0.72	−16.03	14.84	43.92	99.18	5.45	3.08	7.89	98.06
M3	50	1.04	12.16	2.02	−25.88	33.83	−1.42	3.80	0.48	−13.34	7.91	34.63	102.36	4.81	2.74	1.55	81.13
M4	10	6.94	13.91	3.45	−39.81	48.06	−4.46	8.91	1.10	−38.39	11.75	57.99	125.16	9.14	2.27	34.03	136.46
M4	30	8.61	12.43	3.26	−31.91	41.00	−3.62	7.21	0.92	−30.43	14.38	44.41	114.55	10.22	2.41	43.63	103.22
M4	50	9.15	12.92	3.28	−32.08	42.10	−3.48	6.87	0.91	−24.04	19.02	43.91	109.46	9.58	2.63	47.93	107.06
M4	80	4.03	11.02	2.13	−24.98	38.26	−3.43	5.75	1.14	−23.98	9.67	43.28	118.13	5.52	5.83	14.00	77.25
M5	8	2.46	10.59	1.93	−27.97	29.74	−3.82	8.68	1.11	−35.25	22.46	35.47	172.34	5.78	2.84	10.34	93.73
M5	28	6.49	12.00	2.58	−27.78	38.01	−3.51	6.63	1.12	−23.53	13.46	38.04	92.28	8.04	4.98	27.21	94.00
M5	48	5.85	13.06	2.67	−34.78	47.39	−2.85	5.94	1.06	−19.85	11.28	47.95	98.85	7.30	5.61	21.21	102.89
M5	80	0.36	9.43	1.34	−25.65	32.80	−0.64	3.83	0.49	−14.80	14.40	32.88	85.91	3.55	2.87	0.27	51.81
M6	8	4.89	11.06	2.11	−29.25	32.96	−1.40	8.09	0.86	−32.18	24.28	36.42	151.70	6.36	1.98	12.94	93.91
M6	30	10.61	15.71	3.61	−34.23	53.49	−1.61	7.28	1.26	−22.46	21.19	53.57	93.17	9.22	5.25	57.53	149.98
M6	50	9.74	16.45	3.67	−34.14	60.53	−0.62	6.99	1.10	−21.95	22.05	60.64	93.47	8.72	4.34	47.60	159.71
M6	80	1.79	12.34	2.34	−33.94	34.89	0.35	5.63	0.74	−16.18	15.92	35.03	95.30	6.32	3.02	1.66	91.99
M7	53	5.49	16.68	4.79	−37.80	44.06	0.39	9.24	1.62	−28.12	21.77	47.60	112.52	14.03	5.23	15.13	181.80
M7	113	3.28	15.81	4.61	−40.45	35.44	0.30	7.15	1.42	−22.49	26.26	40.46	270.47	14.45	6.76	5.43	150.40
M7	213	−0.52	15.39	4.14	−34.03	29.34	0.46	4.25	0.79	−14.69	16.05	34.11	274.04	12.32	5.93	0.24	127.34
M7	313	−1.50	14.90	3.29	−31.71	27.95	0.19	3.07	0.52	−12.49	9.24	31.74	267.34	8.31	4.97	1.14	115.69
M7	493	−2.53	12.41	2.11	−32.71	26.08	−0.96	1.87	0.25	−6.37	3.97	33.27	259.55	4.92	2.95	3.68	78.79
M8	48	8.49	17.58	4.92	−31.98	57.38	−0.86	10.14	2.22	−34.17	22.07	57.46	87.02	13.33	8.15	36.39	205.84
M8	108	6.19	18.27	5.13	−43.56	45.66	0.23	6.51	1.55	−22.52	22.18	46.37	249.94	13.42	9.67	19.18	188.07
M8	208	1.75	18.17	4.68	−35.74	40.46	0.93	4.16	0.85	−10.43	23.55	40.47	91.50	11.30	7.11	1.97	173.70
M8	308	−0.55	17.75	4.00	−34.52	40.79	0.46	2.91	0.50	−8.14	15.97	40.82	92.16	8.64	4.98	0.26	161.64
M8	498	−1.48	12.49	2.22	−29.77	28.40	−0.26	2.08	0.39	−7.16	4.29	29.78	271.40	5.35	5.85	1.13	80.17
M9	52	10.70	19.53	5.41	−43.58	62.27	−1.06	9.79	1.85	−27.87	35.45	62.36	93.04	13.05	6.09	57.75	238.56
M9	112	5.77	19.52	5.26	−45.63	49.01	−0.89	7.43	1.64	−22.55	25.69	49.92	100.96	12.33	8.25	17.07	217.97
M9	212	−0.52	17.18	4.19	−34.96	34.74	−0.84	5.37	1.28	−23.52	11.97	35.13	264.39	10.12	9.73	0.49	161.95
M9	312	−2.64	17.24	3.52	−40.64	31.83	−0.39	4.62	0.97	−23.49	11.25	40.97	277.32	7.08	7.54	3.55	159.17
M9	492	−6.84	11.21	1.87	−30.64	20.44	0.38	1.04	0.13	−3.81	3.34	30.69	273.32	4.71	2.79	23.48	63.34
M10	47	7.45	18.84	5.25	−45.63	55.36	−2.34	6.99	1.47	−20.09	20.99	55.60	95.38	13.20	7.47	30.47	201.90
M10	97	5.56	21.99	6.31	−55.37	56.74	−2.51	6.82	1.48	−27.29	17.60	58.19	102.96	13.98	7.94	18.62	264.92
M10	197	−1.76	20.55	5.17	−58.89	45.21	−0.55	4.73	0.77	−20.33	15.64	62.29	250.98	10.74	4.49	1.70	222.30
M10	297	−3.96	18.03	3.58	−41.31	42.76	−0.55	3.72	0.57	−17.17	10.54	42.76	89.56	6.70	3.94	8.00	169.36
M10	497	−5.97	8.29	1.29	−24.56	23.03	−1.04	1.47	0.14	−6.26	3.13	24.56	269.49	4.10	1.61	18.38	35.41
M11	48	6.69	17.13	4.56	−55.51	52.13	1.39	9.50	2.00	−19.90	25.90	56.75	283.21	11.95	7.45	23.35	191.74
M11	108	4.29	16.43	4.63	−45.22	37.99	1.56	8.97	2.08	−21.85	39.48	47.15	286.45	13.38	9.05	10.40	175.15
M11	208	1.51	14.29	3.72	−39.41	30.20	2.00	7.74	2.04	−14.85	35.49	42.57	33.83	11.44	11.74	3.14	132.02
M11	308	0.08	12.84	3.24	−35.81	27.92	1.47	4.97	1.27	−9.77	23.26	36.59	257.87	10.71	11.09	1.09	94.69
M11	498	−0.62	10.63	2.47	−33.92	25.90	0.29	2.55	0.52	−10.92	11.14	34.18	262.40	9.07	7.09	0.24	59.70
M11	912	−1.89	4.67	0.79	−15.30	10.45	−0.33	2.01	0.26	−7.31	4.26	15.53	260.03	4.84	2.84	1.85	12.90
M12	48	8.20	19.31	5.07	−44.53	58.13	−0.96	9.85	2.28	−29.47	25.97	58.58	82.87	11.61	9.01	34.06	234.89
M12	108	3.61	17.34	4.55	−44.23	39.28	−0.93	6.80	1.64	−23.69	20.54	44.23	271.06	11.62	9.76	6.96	173.38
M12	208	1.61	15.48	3.86	−41.97	36.31	−1.24	5.67	1.39	−23.64	16.17	42.10	265.35	10.46	10.15	2.07	135.80
M12	308	0.93	14.40	3.60	−38.86	37.59	−1.31	5.32	1.30	−25.42	14.84	41.02	113.72	10.53	10.13	1.30	117.73
M12	498	−0.32	11.53	2.76	−34.50	24.73	−1.08	3.26	0.80	−14.50	5.88	34.54	273.03	9.64	10.08	0.63	71.75
M12	934	−1.88	7.00	1.25	−23.58	11.98	−0.14	1.17	0.14	−3.95	2.95	23.64	266.17	5.38	2.55	1.78	25.17
M13	48	8.02	20.95	5.61	−43.78	60.92	−2.52	9.78	2.36	−32.94	21.28	60.96	91.84	12.07	9.82	35.36	267.09
M13	98	5.14	20.49	5.16	−47.43	47.65	−3.15	9.06	2.32	−32.51	20.14	54.26	238.82	10.69	11.06	18.20	250.89
M13	198	0.22	16.48	4.17	−41.34	32.69	−1.59	5.91	1.35	−32.55	13.28	45.66	244.74	10.80	8.77	1.29	153.27
M13	298	−1.46	13.88	3.19	−34.56	27.95	−0.40	3.93	0.63	−19.70	9.25	35.50	238.60	8.89	4.40	1.15	104.00
M13	498	−2.43	11.43	2.46	−27.32	21.76	−0.42	3.11	0.42	−16.02	8.37	27.67	279.14	7.77	3.08	3.04	70.19
M13	921	−2.80	7.70	1.47	−28.87	17.66	0.38	1.16	0.13	−3.22	4.67	28.95	274.42	6.12	2.11	4.00	30.31

Current components *u* and *v* have been rotated 20° clockwise so that they are approximately parallel and normal to bathymetry contours, respectively. Columns correspond to mooring *M*, measurement depth *Z*, average current component \bar{U} , standard deviation σ_u , standard errors S.E._{*u*}, minimum *u* value *U*_{min}, maximum *u* value *U*_{max}, and similarly for *v*, maximum speed *Spd*_{max}, direction of the maximum speed *Dir*_{max}, integral time scales *IT*_{*u*} and *IT*_{*v*}, mean kinetic energy *MKE* and mean eddy kinetic energy *EKE*. Units in cgs except for integral time scale which is in days.

P1, mean currents were generally upcoast on the shelf and slope. Some downcoast flows were observed below 400 m at M9 and M10 on L3. Maximum average velocity on the shelf was about 19 cm/s at 50 m depth at M6. Maximum average velocity on the slope was 28 cm/s at the 70 m depth at M10. Average velocities progressively increased from west to east in the upper 500 m along L4. Similarly, velocities increased towards the east in the upper 300 m along L3 but then decreased towards the east below 300 m. There was a small offshore component (several cm/s) along all moorings on L1 and L2, and on the eastern ends of L3 and L4 (M9, M10, and M13) while on the slope, this component along the western ends of L3 and L4 (M7, M8, M11, and M12) was nearly zero.

During P2, average currents (Fig. 3) were generally directed downcoast with very weak and highly variable cross-shelf components. Maximum downcoast velocity was about 23 cm/s at 200 m at M10 on L3. During P3, flow had along-shelf and cross-shelf components that were similar in magnitude. Maximum average along-shelf velocity on the shelf was approximately 12 cm/s in the upcoast direction near the surface while maximum cross-shelf currents were about 10 cm/s and directed offshore at M4 on L2. On the slope maximum average upcoast velocity was about

14 cm/s near the surface at M9 on L3 and maximum average downcoast velocity was about 9 cm/s at 450 m depth at M10 on L3. Offshore average velocities between 5 and 10 cm/s were observed along all four lines. During P4, average flow was generally upcoast on the shelf and downcoast on the slope with maximum along-shelf velocities of nearly 20 cm/s observed below 100 m along both L3 and L4. An offshore average flow of about 10 cm/s was observed on the western end of L2 at M4.

The vertically averaged current vectors and standard deviation ellipses at each of the moorings over each of the four time periods are shown in Fig. 4. The center of the standard deviation ellipse is at the tip of the arrowhead and reflects the area that is within one standard deviation of the mean. The stronger mean currents, and best determined currents, occurred during P1, P2, and P4 on the slope along L3 and L4. The depth-averaged currents are not well determined on the shelf since almost all of the current vectors are within the standard deviation ellipses. Additionally, the depth-averaged flow on the outer shelf seemed not to be controlled by bathymetry since the ellipse axes were not constrained by the shelf bathymetry. The principle axis of variability is generally in the direction of the mean flows on the slope, except during P3, which was

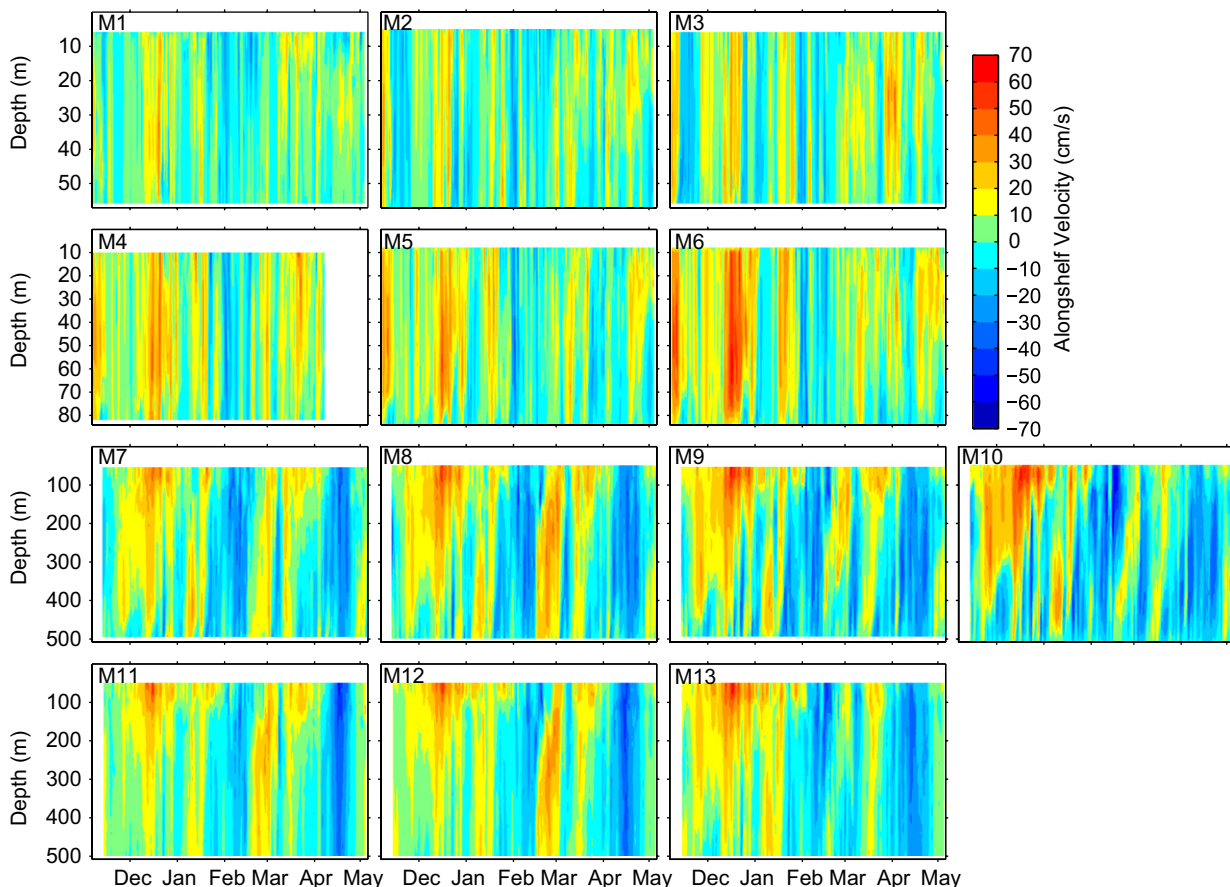


Fig. 2. (a) Velocity time series for the u or along-shelf component. (b) Velocity time series for the v or cross-shelf component. Velocities (cm/s) have been rotated 20° clockwise so that u and v velocity components are approximately parallel and normal to bathymetry contours, respectively. Tides have been removed using a low-pass filter with a 40-h cutoff period.

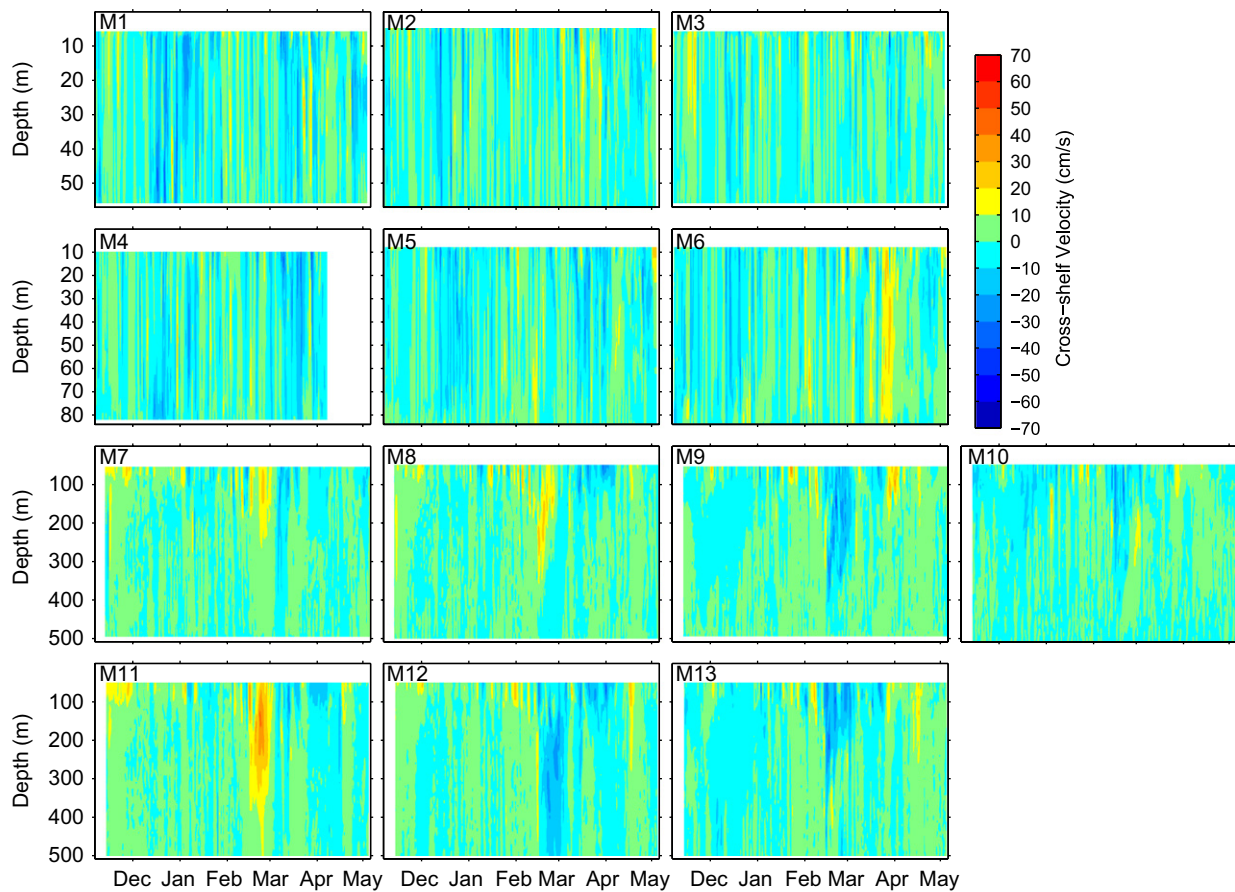


Fig. 2. (Continued)

affected by an eddy that will be discussed later. Otherwise, the depth-averaged currents generally followed the bathymetry on the slope and were polarized in the along-shelf direction much of the time.

For each mooring, vertically averaged flow conditions over the measurement period are further shown by progressive vector diagrams (Fig. 5). The vector diagrams originate at the mooring locations marked by squares. These progressive vector diagrams are suggestive of the direction of the water movement. On the outer shelf, an offshore water movement towards the southeast is indicated at moorings M1–M5, while at M6 the water flows towards the east along the 90 m isobath. On the slope, the water moves generally along the bathymetry and is either upcoast or downcoast, except during the P3 time period. During this period, circulation on the slope was first affected by a cyclonic eddy, which later interacted with an anticyclonic eddy (see Section 8). These interactions appeared to generate an offshore jet, and resulting water movement on the slope was onshore at M8 and M11 on the western ends of L3 and L4, respectively, and offshore at M9 and M10, and at M12 and M13, on the eastern ends of L3 and L4, respectively. In D2, much of the onshore and offshore water movement on the slope can be attributed to these two eddies.

The progressive vector diagrams provided an indication of the along- and cross-shelf water movement. The water movement can be examined more quantitatively using cumulative time integrals of the transports which minimize short-term variability in the long-term trends. Cumulative volume transport (CVT) per unit width versus time at each of the moorings is examined by integrating the depth-averaged velocities from the beginning of the measurement period up to each time in the measurement period and multiplying by the water depth for lines L1–L3, and by 500 m for line L4. CVT provides a comparison of the total volume transported at each mooring along the four lines. CVT for the along-shelf and cross-shelf components of velocity versus time are shown in Fig. 6a and b, respectively. Positive (negative) slopes in CVT are due to persistent trends in upcoast (downcoast) and onshore (offshore) transports. Similar along-shelf trends are observed in CVT along each line (Fig. 6a). On the shelf, the trends are generally upcoast but CVT was much smaller along L1 (M1–M3) than along L2 (M4–M6). The magnitudes of the upcoast and downcoast trends were nearly identical along L3 (M7–M10) until the beginning of P3 (day 415) where CVT at M8 and M10 widely bracket the CVT at M7 and M9, indicating different driving mechanisms. Comparable trend patterns were observed

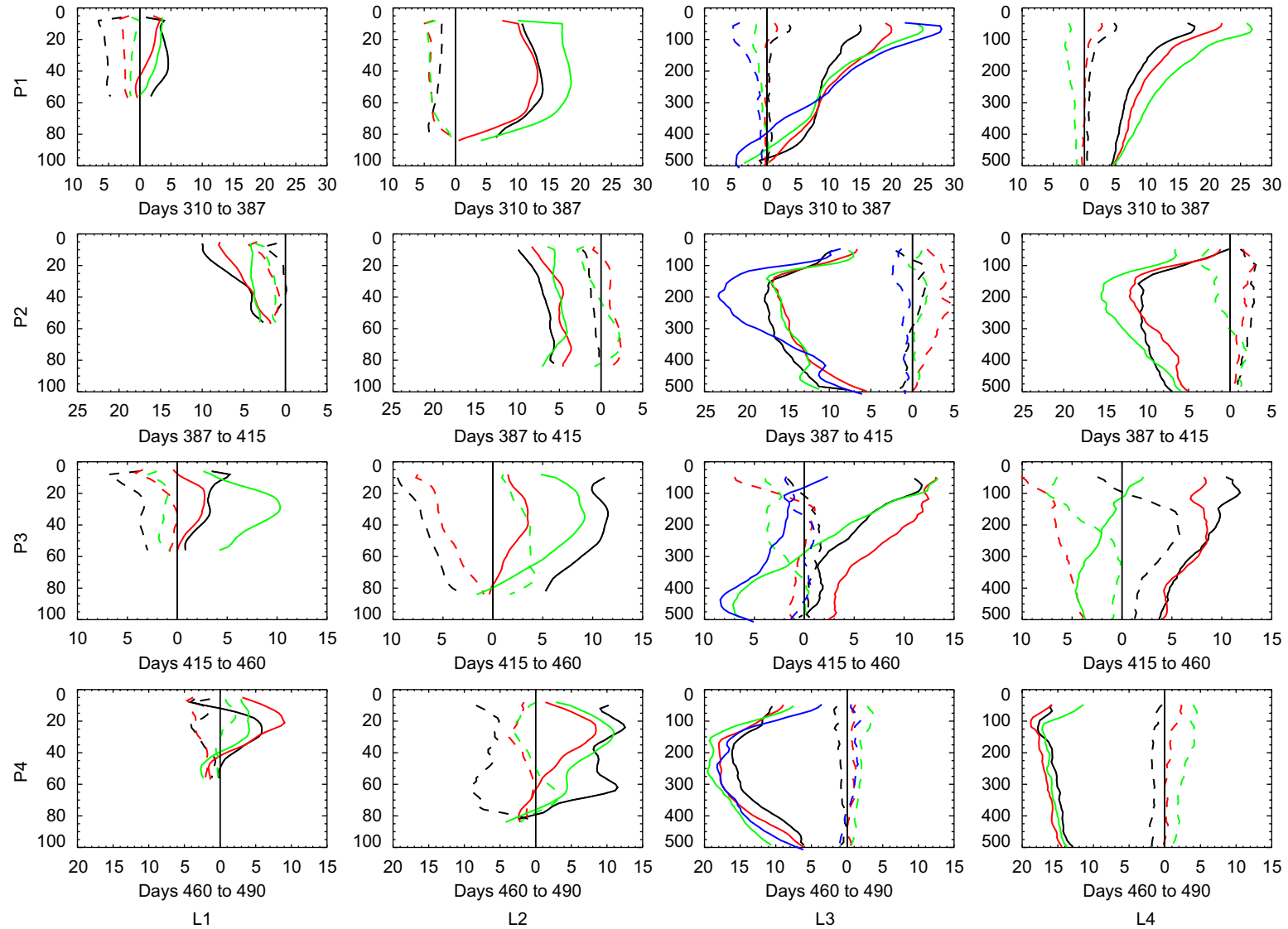


Fig. 3. Time-averaged velocity profiles (cm/s) over depth for four different time periods are shown for each of the four mooring lines. Lines are: L1–M1, M2, and M3; L2–M4, M5, and M6; L3–M7, M8, M9, and M10; and L4–M11, M12, and M13. Time periods are: P1, year days 310–387 (November–mid-January); P2 387–415 (mid-January–mid-February); P3 415–460 (mid-February–March); and P4, 460–490 (April–early-May). Black, red, green, and blue colors correspond to moorings from west to east along each line. Solid lines correspond to along-shelf (u) components and dashed lines correspond to cross-shelf (v) components. Positive u values are upcoast and positive v values are onshore.

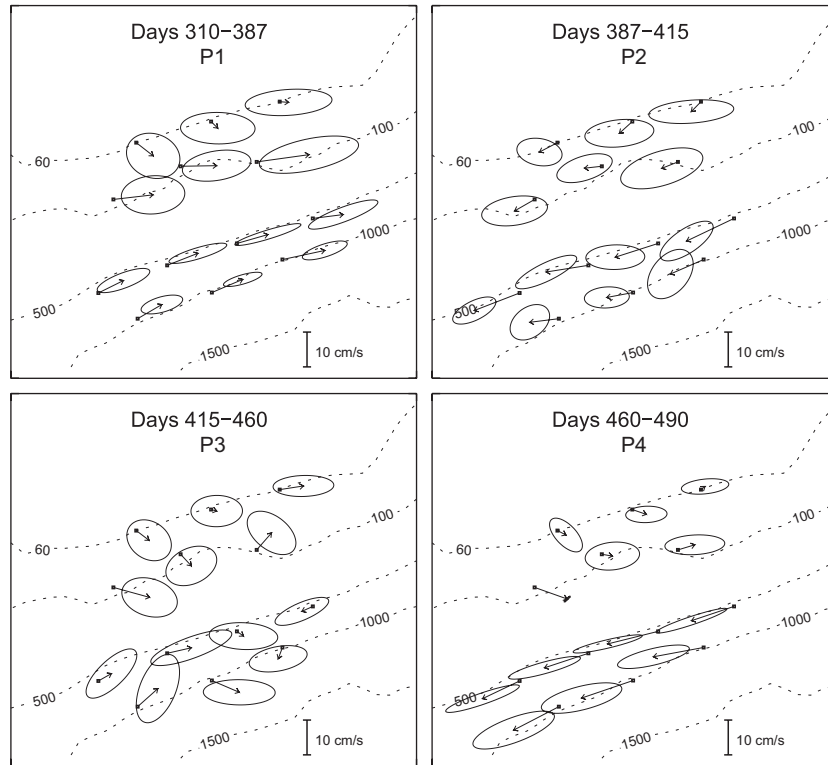


Fig. 4. Mean vertically averaged currents (cm/s) and their corresponding standard deviation ellipses after tide removal are shown at each of the mooring sites. Periods (P1–P4) are described in Fig. 3.

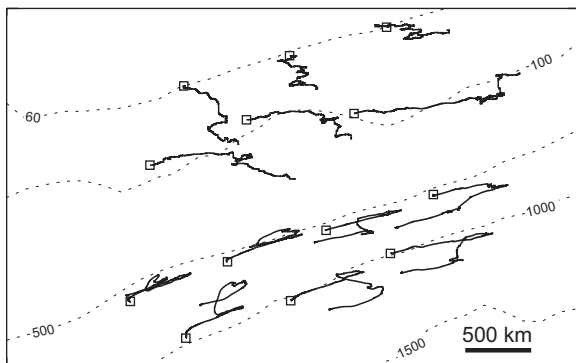


Fig. 5. Progressive vector diagrams for the vertically averaged currents are shown at each of the mooring sites. The vector scale is provided in the lower right corner. Contours of bathymetry in m are dashed.

along L4 (M11–M13). CVT for the cross-shelf component (Fig. 6b) was directed offshore and decreased from west to east along L1. Very similar offshore CVTs were observed between moorings along L2 until around day 420 (start of P3) where CVTs then decreased from west to east. On the slope, onshore and offshore patterns were consistent between lines; onshore at M7 and M8 and offshore at M9 and M10 on L3; onshore at M11 and offshore at M12 and M13 on L4. The range of CVT was about the same for the along-shelf and cross-shelf components along L1 but was smaller for the cross-shelf components along L2 on the shelf, and along L3 and L4 on the slope. To put the observed magnitudes of CVT in perspective, the total

offshore volume of $35 \times 10^6 \text{ m}^3$ accumulated at M5 over 5 months is about seven times the shelf volume per unit width. Hence, the shelf could be emptied in less than a month if this average offshore-directed trend of CVT was uniformly distributed along the shelf.

CVTs were also computed for D1 by Teague et al. (2006). The ranges of the along-shelf components of CVT along the four lines were similar but the ranges of the cross-shelf components were different between the two deployment periods. During D2, cross-shelf CVT ranges were larger and directed offshore on the shelf (Fig. 6b), particularly along L2 (M4–M6) while CVT ranges on the slope were quite similar between D1 and D2. Onshore and offshore transports were likely compensated by the onshore and offshore flows associated with eddies on the slope. However, increased eddy activity (see Section 8) during D2 may have had more of an impact on L2 on the shelf, resulting in onshore and offshore transports, and on L3 and L4 near days 410 (mid-February) and 470 (mid-April). Hence, along-shelf components of CVT appear to be mainly driven by winds but the cross-shelf CVTs were enhanced by eddies during D2.

5. Barotropic currents

Much of the analyses performed here utilized vertically averaged currents. To quantify how representative these averaged currents are to the circulation patterns, the ratio of the mean depth-dependent *EKE* to the total *EKE*

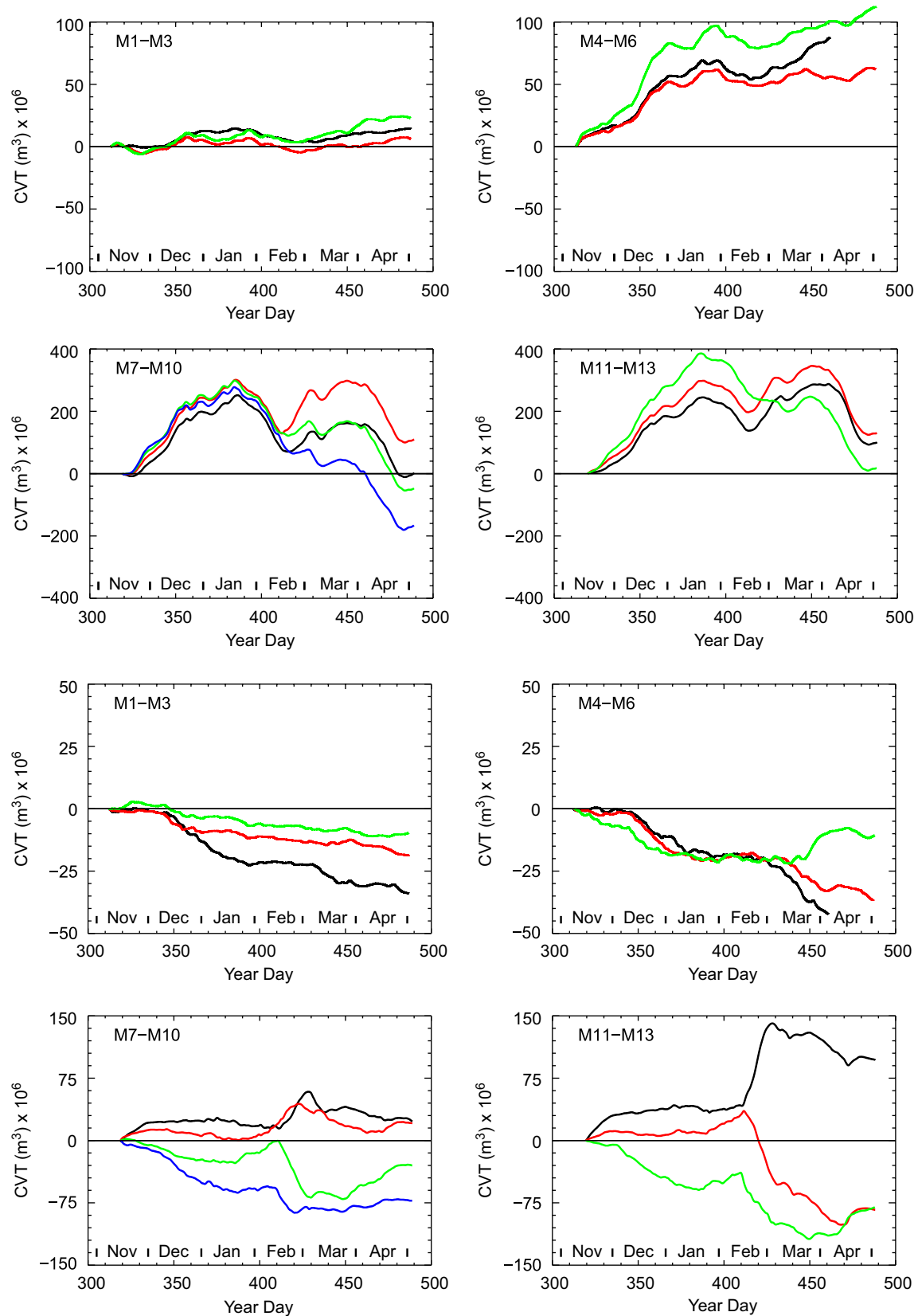


Fig. 6. Cumulative volume transported (CVT) per unit width versus time is shown for the measurement period. CVT is formed by integrating the depth-averaged velocities from the beginning of the measurement period up to each time in the measurement period and multiplying by the water depth for M1–M10 (L1–L3) and by 500 m for M11–M13 (L4). (a) Along-shelf component (u). (b) Cross-shelf component (v). Black, red, green, and blue colors correspond to moorings from west to east along each line.

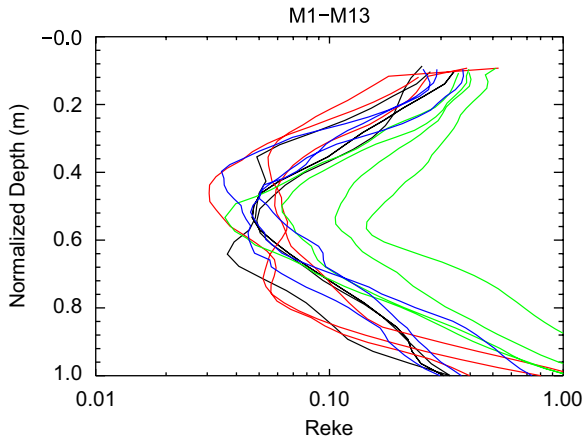


Fig. 7. Ratios of the time mean over D2 of depth-dependent eddy kinetic energy to the total eddy kinetic energy are shown for the moorings along each of the 4 lines. Black, red, green, and blue colors correspond to moorings along lines 1–4, respectively. Depths have been normalized by the maximum depth of each velocity profile. Magnitudes of R_{cke} are given in a log scale on the x -axis. Low values of R_{cke} correspond to high barotropy.

was calculated (see Teague et al., 2006 for details). R_{cke} is given by

$$R_{cke}(z) = \left(\overline{u'^2_{dd}}(z) + \overline{v'^2_{dd}}(z) \right) / \left(\overline{u'^2}(z) + \overline{v'^2}(z) \right),$$

where $\overline{u'^2_{dd}}$ and $\overline{v'^2_{dd}}$ are the variances of the depth-dependent components of velocity and $\overline{u'^2}$ and $\overline{v'^2}$ are the total velocity variances. The average R_{cke} during D1 was 0.13 and indicated that the dominant processes were highly barotropic. Profiles of R_{cke} are shown for each mooring during D2 in Fig. 7. The depth has been normalized for L1–L4 by the depth of the deepest velocity bin which is approximately the water depth for L1–L3 and 500 m for L4. These profiles show the relative contributions of the depth-dependent mean EKE to the total mean EKE . Similar to those in D1, the profiles are “C” shaped and show low values of R_{cke} for mid-depths, encompassing about one third of the water column. Hence, EKE was almost entirely barotropic in the middle layer. The overall average of R_{cke} for all four lines is 0.20 and is suggestive that barotropic processes accounted for about 80% of the energy, a little less than during D1. Baroclinic processes had a greater effect on the slope along L3 but not on the deeper part of the slope along L4. Barotropic processes along L3 accounted for about 70% of the energy. The larger baroclinic contribution along L3 suggests that the exchange processes are larger, at least for the upper 500 m, along the upper slope. The gradients in R_{cke} in the top and bottom layers are likely associated with surface and bottom Ekman boundary layers or buoyancy effects due to rivers. The current in the bottom Ekman layer associated with an upcoast (downcoast) geostrophic flow turns to the left as the bottom is approached, resulting in an onshore (off-shore) cross-shelf exchange. Liu and Weisberg (2007) suggest that the flow in the bottom Ekman layer is an

important contributor to cross-shelf exchange on the west Florida shelf.

6. EOF analysis

To better understand the regional picture of the low-frequency currents in the SEED region during the winter and spring periods, it is preferable to analyze groups of moorings instead of individual moorings. Therefore, EOFs were calculated in hope of extracting dominant spatially correlated variability on the shelf and slope with just a couple of EOFs. The approach is similar to that presented in Teague et al. (2006). Velocity EOF modes were computed from the de-meaned, but unscaled, combined east-west and north-south components of vertically averaged velocity using data from three different groupings of the moorings. The individual vertically averaged time series were not normalized by their standard deviations, as is often recommended (Preisendorfer, 1988), because of the small range in the standard deviation of the speeds among the moorings. This approach allowed the eigenvectors to be interpreted directly since their relative magnitudes are maintained without rescaling with their individual standard deviations. Vertical averaging for each mooring was computed over the entire depth range of the ADCP observations. The first set uses all 13 moorings, the second set uses only moorings located on the shelf (M1–M6), and the third set uses moorings located over the slope (M7–M13). M4 was excluded from the second set, but not the first set, because its time series ended on April 3, 2004, 26 to 27 days earlier than the other shelf mooring. Because of the different deployment and recovery times for the moorings, the EOF analyses were performed over different time periods for the three sets. EOFs were computed from November 18, 2004 to April 3, 2005 for the full mooring set, from November 11, 2004 to April 29, 2005 for the shelf set, and from November 18, 2004 to April 30, 2005 for the slope set.

The cumulative percent of variance explained versus the number of EOFs for each of three sets of moorings is shown in Fig. 8. Each plot shows a line for the total cumulative percent of variance (combined u and v variances), the cross-shelf percent (v variances), and the along-shelf percent (u variances). The u and v components of the velocity were rotated prior to calculation of variances to the vector average direction of mode 1 EOFs, weighted by their magnitudes, for each of the three sets of moorings. The velocities were rotated so that the positive u component lies along $78.4^\circ T$ for the complete mooring set, $84.9^\circ T$ for the shelf mooring set, and $72.8^\circ T$ for the slope mooring set. Much of the velocity variance is contained in the along-shelf velocity component. The total cross-shelf variance is only 13.3%, 16.4%, and 6.7% of the combined along-shelf and cross-shelf variance for the total, shelf, and slope mooring sets, respectively. Furthermore, only a small fraction of the cross-shelf velocity variance is explained by the first few EOFs for the total and shelf sets. However,

mode 2 EOF of the slope set explains about 35% of the cross-shelf variance. As discussed later, this cross-shelf variability captured by mode 2 is related to a period of slope eddy intrusions. The first mode EOFs account for 56%, 62%, 84% of the combined u and v variance for the total, shelf, and slope data set, respectively, indicating a very uniformly varying flow over the slope, and more localized variability on the shelf. A vector velocity time series at each mooring constructed from a single EOF is restricted to vary in a rectilinear back and forth motion, according to the amplitude time series for that EOF. Although the direction and magnitude of the EOF vectors can be different at each mooring, they all share the same amplitude time series. Therefore, a dominant first EOF mode indicates a highly correlated in-phase motion across the set of moorings.

The test developed by Overland and Preisendorfer (1982) to distinguish EOF modes from noise indicates that only the first three EOFs for the full mooring set and first two EOFs for the shelf and slope data sets have variances different from those expected from random noise at the 95% significance level. EOF 3 from the combined shelf and slope data set and EOF 2 from both the shelf data set and the slope data set just barely passed this test. However, the amplitude of EOF 2 was small during the time series except during the passage of two eddies where EOF 2 played a significant role (see discussion later in this section). Based

on these results, only the first two EOFs for all three data sets are used in subsequent analysis. The variance is broken down further to examine the percent of variance explained by the combined first two EOF modes at each mooring for the rotated u -component (along-shelf), v -component (cross-shelf), and the combined u and v components. The variance distributions for the full, shelf, and slope mooring sets are shown in Fig. 9. For the full mooring set (Fig. 9, left frame), the first two EOFs explain an average of only 7% and 22% of the cross-shelf velocity variance and an average of 72% and 87% of the along-shelf variance for the shelf and slope, respectively. Even when the EOF analysis is performed using only the shelf (Fig. 9, center frame) or slope (Fig. 9, right frame) set of moorings, the explained cross-shelf variance percentages remain low, but along-shelf percentages increase substantially. Cross-shelf flow variability is poorly correlated among shelf moorings in addition to being poorly correlated between shelf and slope moorings. In the slope mooring set, the along-shelf variance percentages are uniformly high, but the cross-shelf variance percentages have a large range, probably due to intrusions of slope eddies (as will be discussed below).

The large-scale features of the correlated flows are shown using EOF vector maps. Maps of the vectors for each of the first two EOFs for each of the data sets are shown in Fig. 10. The shelf and slope sets are shown individually in order to isolate the processes common to each region. The

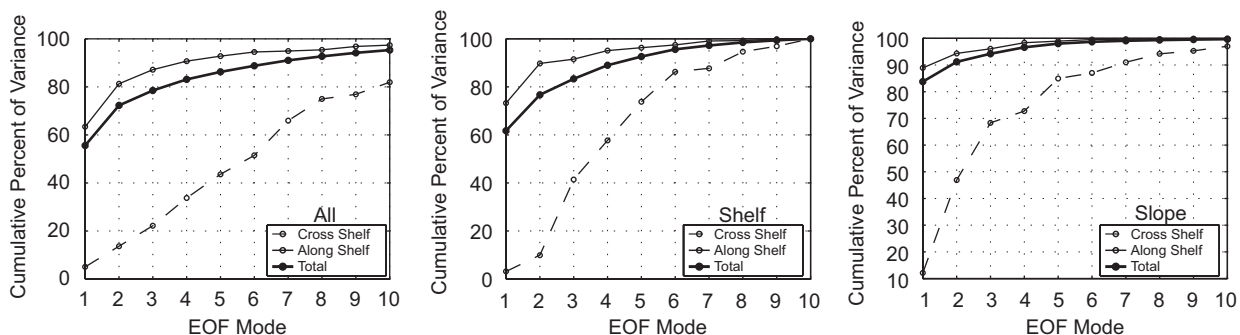


Fig. 8. Cumulative percent of variance explained versus the number of EOFs for each of three sets of moorings for the cross-shelf and along-shelf velocity components and for the total velocity. The velocity data set used for each case (all, shelf, and slope) were assembled from mooring M1–M13, M1–M6, excluding M4, and M7–M13, respectively.

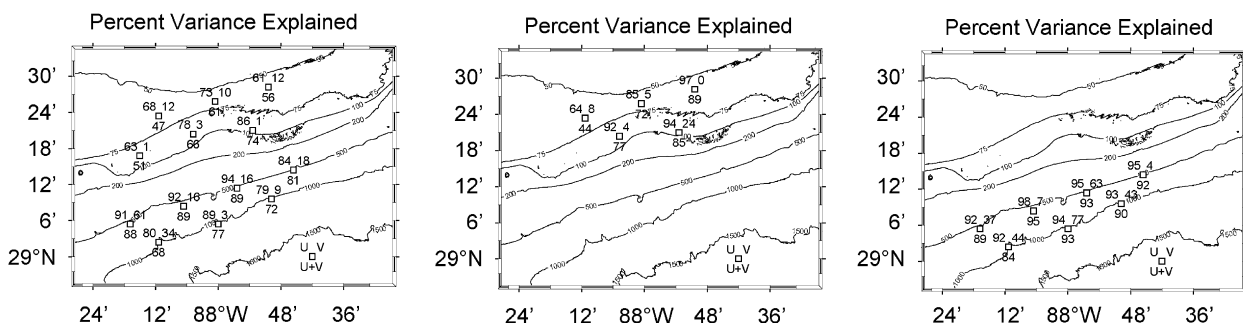


Fig. 9. Distribution of the explained variances at each of the moorings from the first two EOF modes is shown for each of the three sets of moorings (all, shelf, and slope). The variances, which are displayed at the upper left and upper right, and below each mooring position, correspond to the east-west variance, the north-south variance, and the combined variance, respectively.

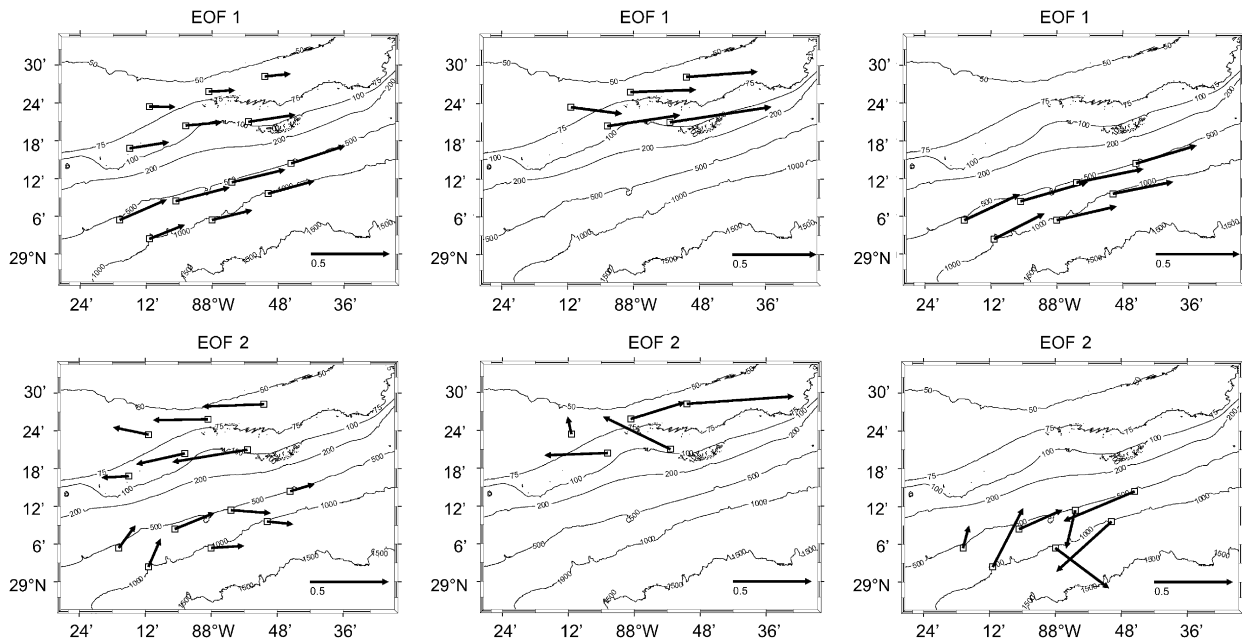


Fig. 10. Vector EOFs of the vertically averaged velocity for the first mode (first row) and second mode (second row) for the full set (left), shelf set (middle), and slope set (right) of moorings. The normalized magnitude scale is displayed in the lower right corner of each plot.

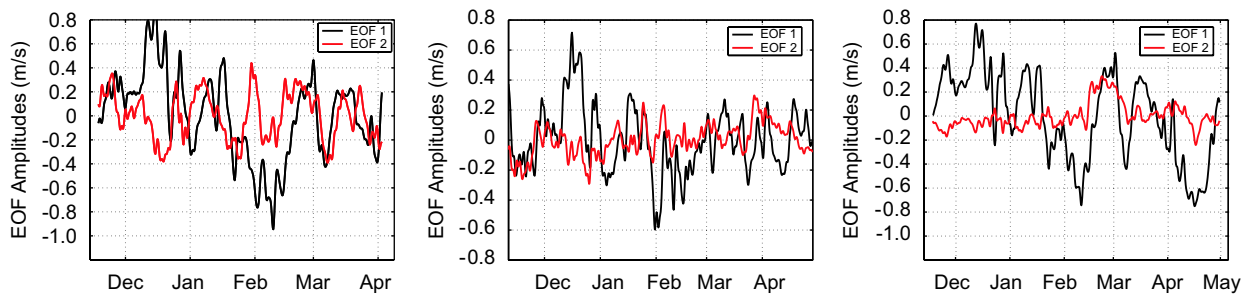


Fig. 11. Amplitudes versus time for mode 1 (black line) and mode 2 (red line) EOF for the full mooring set (left), shelf set (middle), and slope set (right).

vector fields for the first and second modes for the total data set are similar to those for the summer period shown in Teague et al. (2006). The vectors for each mode are normalized such that the sum of squares of the velocity components over all moorings is unity. Mode 1 currents are aligned approximately in the same direction for each data set, nearly parallel to the isobaths. To maintain constant volume, the divergence (convergence) produced by the 12.1° angle difference between shelf (84.9°T) and slope (72.8°T) currents must produce an eastward acceleration (deceleration) of the currents between lines 2 and 3 when the currents are directed eastward (westward). The shelf currents are weaker than those over the slope, but the currents are strongest on the two central lines (L2 and L3), closest to the shelf break, than on the two outer lines (L1 and L4). For the full-mooring data set, mode 2 currents on the shelf are in the opposite direction to those over the slope, and have only a small cross-isobath component. Mode 2 vectors for the individual shelf and slope data sets exhibit strong along-shelf divergence and significant cross-

shelf velocity. The second mode from the slope data sets exhibits a clockwise rotation of vectors on the western half of the array and a counter-clockwise rotation on the eastern half. This rotation could be attributed to an eddy intrusion along the slope that will be addressed later.

Time series of the amplitudes of the first two EOFs are shown in Fig. 11 for each of the three sets of moorings. For the full set, the shelf set, and the slope set (Fig. 11), the first mode amplitudes show several large peaks with widths of about 2–3 weeks (mid-December, mid-January, early March, and mid-March). Superimposed on the peaks is a general downward trend in amplitudes for the first mode from about mid-December to mid-February. The downward trend in the shelf set is weaker than in either the full set or the slope set, and the peaks in the second half of the series are nearly missing or indistinguishable. Hence, statistical analysis suggests that different forcing mechanisms dominate the shelf and slope processes. The time series exhibit fluctuations with time scales from a few days to a month and variations with seasonal time scales.

7. Local wind stress—simple Ekman balance

In this section the change in total along-shelf momentum per unit mass and per unit area are compared to the net momentum added at the surface by wind stress minus the momentum removed at the bottom by friction. The physics of this balance on the shelf and slope has been studied for cases where the shelf bathymetry is simple, particularly where the coastline is straight and the bottom depth is a simple function only of the distance offshore (Csanady, 1974). The vertically integrated Ekman transport equation with the Coriolis term set to zero

$$\frac{\partial u}{\partial t} = \frac{\tau_s^x - \tau_b^x}{\rho H} \quad (2)$$

was shown in several studies (Lentz and Winant, 1986; Hickey et al., 2003; Jarosz and Murray, 2005) to model the flow well, even over the deeper shelf. In Eq. (2), u is the vertically averaged along-shelf current, H is the bottom depth, ρ is vertically averaged water density, τ_s^x is the surface stress due to wind in the x direction, and τ_b^x is the bottom stress in the x direction. When the bottom stress is assumed to be proportional to the vertically averaged along-shelf current, $\tau_b^x = r\rho u$, where r is the resistance coefficient, Eq. (2) can be integrated to obtain

$$u(t) = u(0) \exp(-rt/H) + \frac{1}{\rho H} \int_0^t \tau_s^x \exp\left(\frac{-r(t-t')}{H}\right) dt'. \quad (3)$$

The bathymetry of the shelf and slope in the vicinity of the moorings is reasonably simple (straight and uniform). The broader shelf is bounded on the west (about 80 km away) by the Mississippi delta, on the north (about 100 km away) by the Alabama and Mississippi coastline, and on the east by the Desoto Canyon (see Fig. 1). In addition, the shelf break is aligned nearly 20° counter-clockwise to that of the northern coastline. Due to these complications, the most effective wind stress may not be directed alongshore and the relationship between the wind stress and the along-shelf currents are not necessarily well represented by Eq. (2). For example, Shearman and Lentz (2003) found that the alongshore currents on the New England shelf responded most strongly to the wind stress component oriented nearly across shore, approximately in line with the large-scale orientation (1000 km) of the coastline. Hence, we examined the correlations between the time series of composites of the along-shelf detrended vertically averaged currents, u' (described below), and the predicted current, p , from the wind stress. The time series for p is computed from a generalization of the integral from Eq. (3),

$$p(t) = \int_0^t \tau_s^\theta \exp\left(\frac{t'-t}{D}\right) dt', \quad (4)$$

where $\tau_s^\theta = \tau_s^x \cos(\theta) + \tau_s^y \sin(\theta)$ is the component of wind stress in the direction, θ , and D is the e-folding decay time scale. The integral in Eq. (4) is not scaled by ρH as it was in

Eq. (3) since this factor does not affect the correlation of p with u' . The hourly values of wind stress computed from the winds measured at the NOAA Buoy 42020 (Fig. 1) near the moorings were used in the integration. The integration was started at a time well before the beginning of the current observations so that the initial boundary condition term (first term in Eq. (3)) could be ignored. Predicted time series were computed from Eq. (4) for a matrix of D and θ values (usually D from 0 to 14 days with increments of 0.25 days and θ from 0 to π to with increments of $\pi/90$). Each predicted series was then filtered using the same 40-h low-pass filter that was applied to the measured currents.

Four composite time series of the low-pass filtered along-shelf vertically averaged currents, u' , were prepared, one each for the shelf and slope moorings for both D1 and D2. To form each composite, the 40-h low-passed along-shelf component time series from each mooring was first vertically averaged. Then, all resulting vertically averaged time series from either the shelf set or the slope set of moorings and for either the D1 or D2 deployments were averaged together. Each of the resulting four composite time series was detrended to remove seasonal, long-period, fluctuations using a fourth-order polynomial, computed over the time period of each of the mooring velocity time series to form the final measured current series, $u'(t)$. The detrending performed as expected for each case by removing the long period seasonal trends and retaining only the fluctuations in the central (weather) frequency band (40 h to about 1 month). The seasonal trend was removed from the measured current since the predicted current is calculated from the wind stress based on a typical decay time scale of about a week. Only the subset from June 1 to September 4, 2004 of the time series from D1 was used in order to eliminate measurements during passage of an eddy (referred to as E1 later) at the beginning of the series and to eliminate effects of Hurricane Ivan at the end of the series. For D2, the full shelf data set (excluding mooring M4 because it ended early) was used, but the slope data set was terminated on February 10, 2005, prior to the passage of a series of eddies (E2, E3, and E4, discussed in the next section). The full depth range of measured currents was used in the vertical averages for the shelf moorings, but the depth range for averaging over the slope was limited in order to maintain higher predictability from wind stress while still using as much of the water column as possible. Correlations between wind stress and depth-averaged currents were computed using the procedure outlined in the next paragraph for several different depth ranges. Based on these tests over the slope, the depth range from 50 m (the upper level of the ADCP measurements over the slope) to 200 m (the most baroclinic portion of the upper profiles, see Fig. 7) was used in the vertical average for D1 and D2.

Correlations between the measured u' series and the corresponding (D , θ) matrix of the predicted p series were computed. The results are shown in Fig. 12a–d by contours of correlation as functions of decay time scale and wind

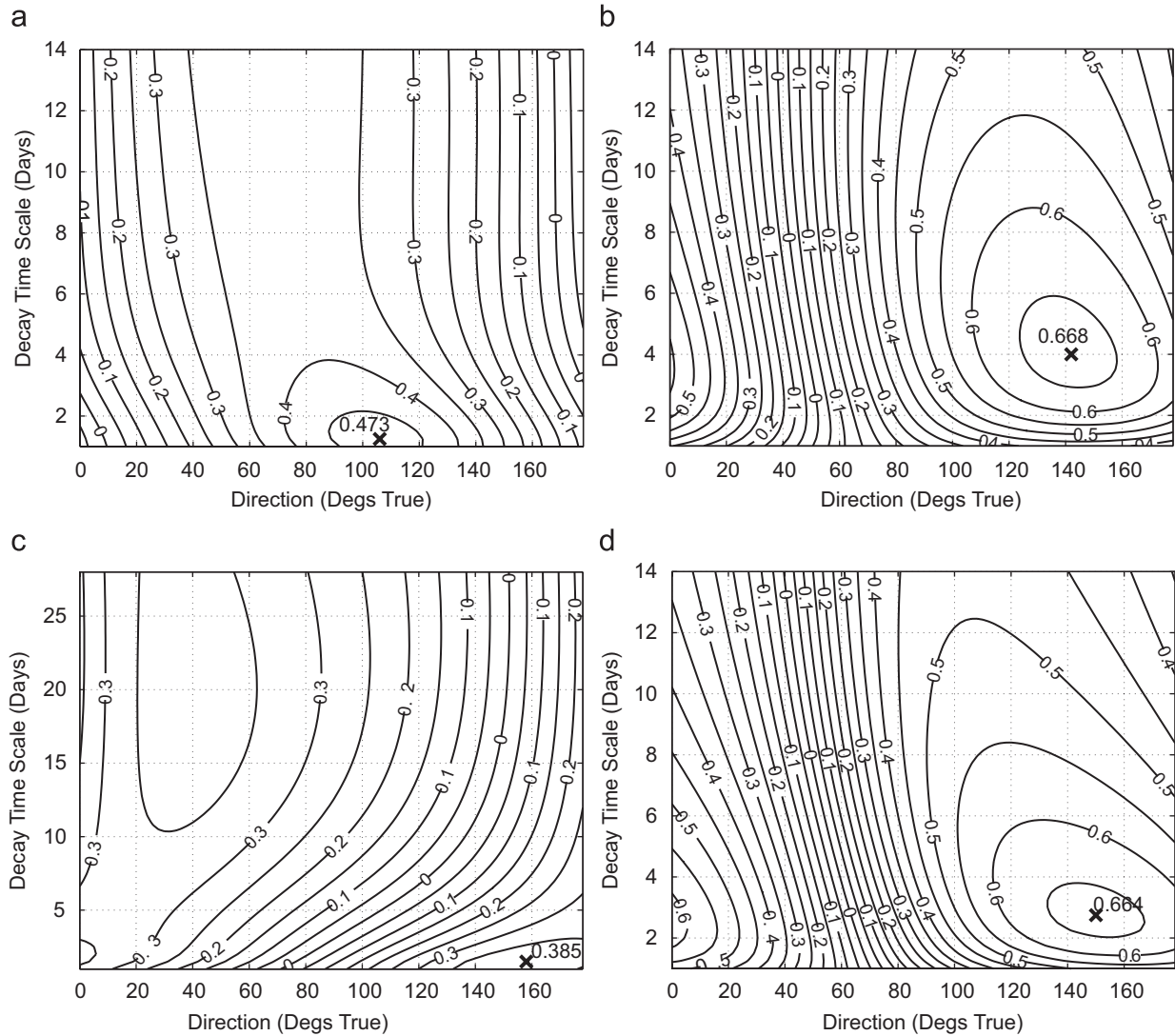


Fig. 12. Contour plots of correlation between detrended along-shelf vertically averaged velocity and the velocity predicted from the vertically integrated Ekman equation, Eq. (2), using local wind stress from NOAA Buoy 42040 for (a) the shelf during D1, (b) the shelf during D2, (c) the slope during D1, and (d) the slope during D2. Correlation is plotted as a function of decay time scale in days and direction of the wind stress component in degrees True. The symbol, x, marks the position of maximum correlation on each plot.

Table 3

Values obtained and computed from Fig. 12, at the point of maximum positive correlation between the measured and predicted vertically averaged current on the shelf and slope for D1 and D2

	Shelf D1	Slope D1	Shelf D2	Slope D2
Correlation	0.47	0.39	0.67	0.66
D (days)	1.25	1.5	4	2.75
θ ($^{\circ}$ T)	106	158	142	150
$\sigma_{u'}$ (m/s)	4.43×10^{-2}	4.12×10^{-2}	8.60×10^{-2}	6.64×10^{-2}
σ_p (kg/m/s)	1.93×10^3	2.67×10^3	9.21×10^3	8.62×10^3
H (m)	43	63	104	127
r (m/s)	3.9×10^{-4}	4.9×10^{-4}	3.0×10^{-4}	5.3×10^{-4}

Listed values include the correlation between u' and p , the decay timescale, D , the wind stress component direction, θ , the standard deviation of the measured series, $\sigma_{u'}$, standard deviation of the predicted series, σ_p , the layer depth, H , estimated from the ratio, $\sigma_p/(\rho\sigma_{u'})$, and the resistance coefficient, r , estimated from H/D .

stress direction. Table 3 lists several parameters found at the point of maximum correlation for each case. The maximum correlations were over 0.66 for both shelf and slope in D2, but were only 0.47 and 0.39 for the shelf and slope, respectively, in D1. The correlations for the shelf and slope cases for D2 are significantly different from zero at the 95% confidence level, but for the D1 case, the shelf correlation is marginally significant and the slope correlation is not significant. Climatologically calculated mixed layer depths (Mendoza et al., 2005) are generally less than 50 m for the time period associated with D1. Since the uppermost measured velocities on the slope are about 50 m, the low correlation on the slope during this period is not surprising.

The decay time scales at maximum correlation ranged from 1.25 to 4 days over both deployments. During D2, the wind stress direction at maximum correlation was 142 and

150°T, towards the southeast on the shelf and slope, respectively. Mode 1 EOF weighted average current directions were found above to be about 85°T over the shelf and 73°T over the slope, approximately in line with the isobaths. Therefore, these wind stress orientations were 57° and 77° clockwise from the isobath direction. This oblique angle is contrary to the simple theory (Lentz and Winant, 1986) which states that the along-isobath currents respond most strongly to the along-isobath component of the wind stress. However, other studies have also found that the highest correlations between along-isobath currents and the wind stress occurred at oblique angles to the isobaths (Shearman and Lentz, 2003; Beardsley et al., 1985). They concluded that the wind forcing parallel to the orientation of the coastline on length scales larger than 1000 km was most effective at driving the along-isobath flow. Here, the orientation of the West Florida shelf is about 150° over a distance of about 500 km between Cedar Keys and Cape Sable. Hence, west Florida shelf currents, such as generated by shelf waves (Hsueh and Golubev, 2002), continuing on into SEED region may contribute to the current variability.

Estimates of the effective layer depth, H , and resistance coefficient, r , can be obtained from simple relationships obtained by comparison of Eqs. (3) and (4). By matching the standard deviations of the measured ($\sigma_{u'}$) and predicted (σ_p) series, we obtain $H = \sigma_p / (\rho \sigma_{u'})$, and then $r = H/D$. Values for these parameters are listed in Table 3. During D2, when the water column was well mixed to the bottom, the value of H (104 m) on the shelf agrees well with the bottom depths along the two lines of shelf moorings at 60 and 90 m. During D1, when summer heating produced a strong mid-depth thermocline, the value of H was shortened to 43 m. Estimates of H over the slope, where the bottom depths are from 500 to 1000 m at the mooring locations, were comparable to the shelf estimates but approximately 20 m larger. The resistance coefficient estimates range from 3.0×10^{-4} to 5.3×10^{-4} m/s, which compared favorably to the often used value of 5.0×10^{-4} m/s (Hickey et al., 2003).

Plots of the measured and predicted (modeled) time series are shown in Fig. 13. For each of the four cases, the measured and predicted series scaled by their standard deviations, $u'/\sigma_{u'}$ and p/σ_p , respectively, are plotted in the

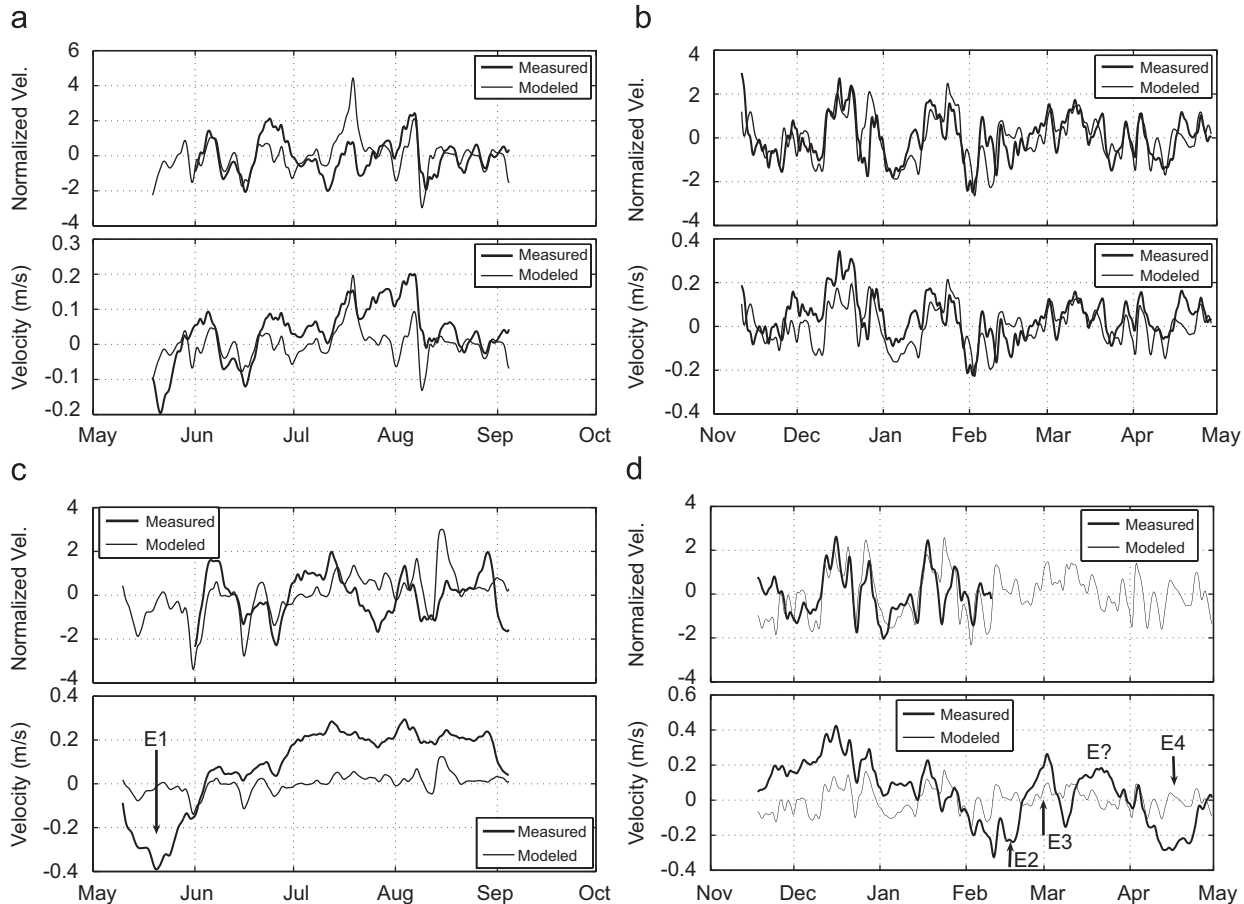


Fig. 13. Observed and predicted time series of vertically averaged along-shelf current for (a) the shelf in D1, (b) the shelf in D2, (c) the slope in D1, and (d) the slope in D2. The upper frame for each set shows the observed (measured) and predicted (modeled) time series scaled by their standard deviations and with the fourth-order polynomial trend removed from the observed series. The bottom frame for each set shows the full measured multi-mooring average of along-shelf velocity and the re-scaled predicted velocity. The symbols E1–E4 indicate times when eddies passed through the slope moorings as determined from satellite images of sea surface temperature and chlorophyll concentration, discussed in Section 8. Eddy E3 is anticyclonic and E1, E2, and E4 are cyclonic. The symbol E? indicates possible impingement by an anticyclonic eddy not seen in the images.

upper panels and the measured velocity (40-h low-pass filtered), u , and the reconstructed velocity predicted from the wind stress computed as, $p\sigma_u/\sigma_p$, are plotted in the lower panels. The symbols, E1–E4 on the lower panels of the slope series, indicate times when eddies (discussed in Section 8) identified from remotely sensed sea-surface-temperature and chlorophyll imagery impinged on the slope moorings. Dominant periods of variability range from about 1 to 2 weeks in D1, while the periods range from a few days to a month in D2. The low correlations in D1 (marginal on the shelf and not significant on the slope) are visually apparent in the comparisons between the scaled observed and predicted series shown in Fig. 13a and c (upper panels). In D2 the correlations are relatively high (and statistically significant) on both the shelf and slope as evidenced by the close agreement between the scaled time series (Fig. 13b and d, upper panels). When the series are rescaled and the seasonal fourth-order polynomial trend is included (Fig. 13, lower panels), large seasonal trends of 0.2–0.3 m/s are revealed in the differences between the observed and predicted series. The seasonal trend, as expected, results primarily from addition of the polynomial trend removed earlier. The magnitudes of the seasonal trends are larger on the slope than on the shelf during both D1 and D2. The seasonal trend may be predictable from the wind stress, but only if a much longer decay time scale is used. Thus there can be two different processes at work on the shelf and slope controlled by the wind stress: one producing fluctuations on the order of a week or two and the other on seasonal time scales or longer. The seasonal trends are discussed in Section 9.

Calculations were also performed for both deployments to determine the relationship between the cross-shelf vertically averaged velocity and the wind stress (not shown in Table 3). The maximum correlations for the shelf and slope time series were statistically insignificant for both deployments.

8. Slope eddies

Daily MODIS (Moderate Resolution Imaging Spectroradiometer) 1-km (Level 2) images of sea surface temperature and chlorophyll concentration were examined over both deployments for evidence of eddies. Clouds obscured the shelf and slope region surrounding the mooring array on many days. However, enough partial and full images were available to identify three periods showing four eddies that had substantial impact on the slope moorings. The periods when each of these eddies passed through the mooring array are marked by the E1 symbol in Fig. 13c and by E2–E4 in Fig. 13d.

The first eddy (E1; Fig. 14) was visible in chlorophyll images on May 13 and May 18, 2004 during the period when the along-shelf velocity reached a westward peak on both the shelf and slope (Fig. 13a and c, respectively). It was the only eddy observed to pass through the mooring array during D1. The center was located south of the moorings over a bottom depth between 1500 and 2000 m. It

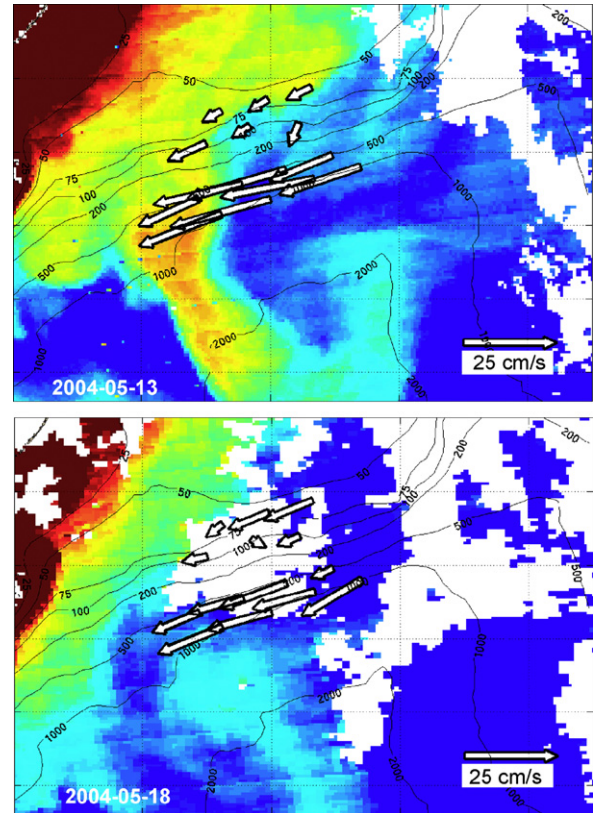


Fig. 14. MODIS color images showing \log_{10} of the chlorophyll concentration at 1-km resolution showing passage of a cyclonic eddy (E1) along the slope during D1. Highest concentrations are red and lowest are blue. Vertically averaged currents are shown projecting from each mooring location. The vector velocity scale (25 cm/s) is shown in the lower right corner. White areas are masked by clouds.

was cyclonic as indicated by the streamer in the upper frame of Fig. 14, had a radius of about 60 km, and moved westward at about 0.09 m/s between the first and second images. The vertically averaged currents at the time of each image are drawn with the tail at each mooring location. The peak vertically averaged (upper 500 m) westward along-shelf velocities of 0.15 m/s on line L1, 0.25 m/s on L2, 0.41 m/s on L3, and 0.36 m/s on L4 were reached between May 19 and May 22.

A 1-month sequence of 12 images of sea surface temperature in Fig. 15 shows the interaction of a cyclonic eddy with an anticyclonic eddy as they propagated on the slope and impinged on the moorings. The sequence begins on February 2, 2005 with a cyclonic eddy (E2) situated east of the moorings over the DeSoto canyon. In the next five images from February 14 to February 19, the eddy moved westward, causing the velocity on the eastern end of the mooring array to turn southward. On February 18 and February 19 the eddy appeared to be squeezed in the north-south direction by the northward encroachment of the Loop Current, visible as the northward arch of dark red (higher temperatures) at the bottom of the images. The next good image (March 1) also shows an anticyclonic eddy (E3) centered south of the moorings. Its appearance

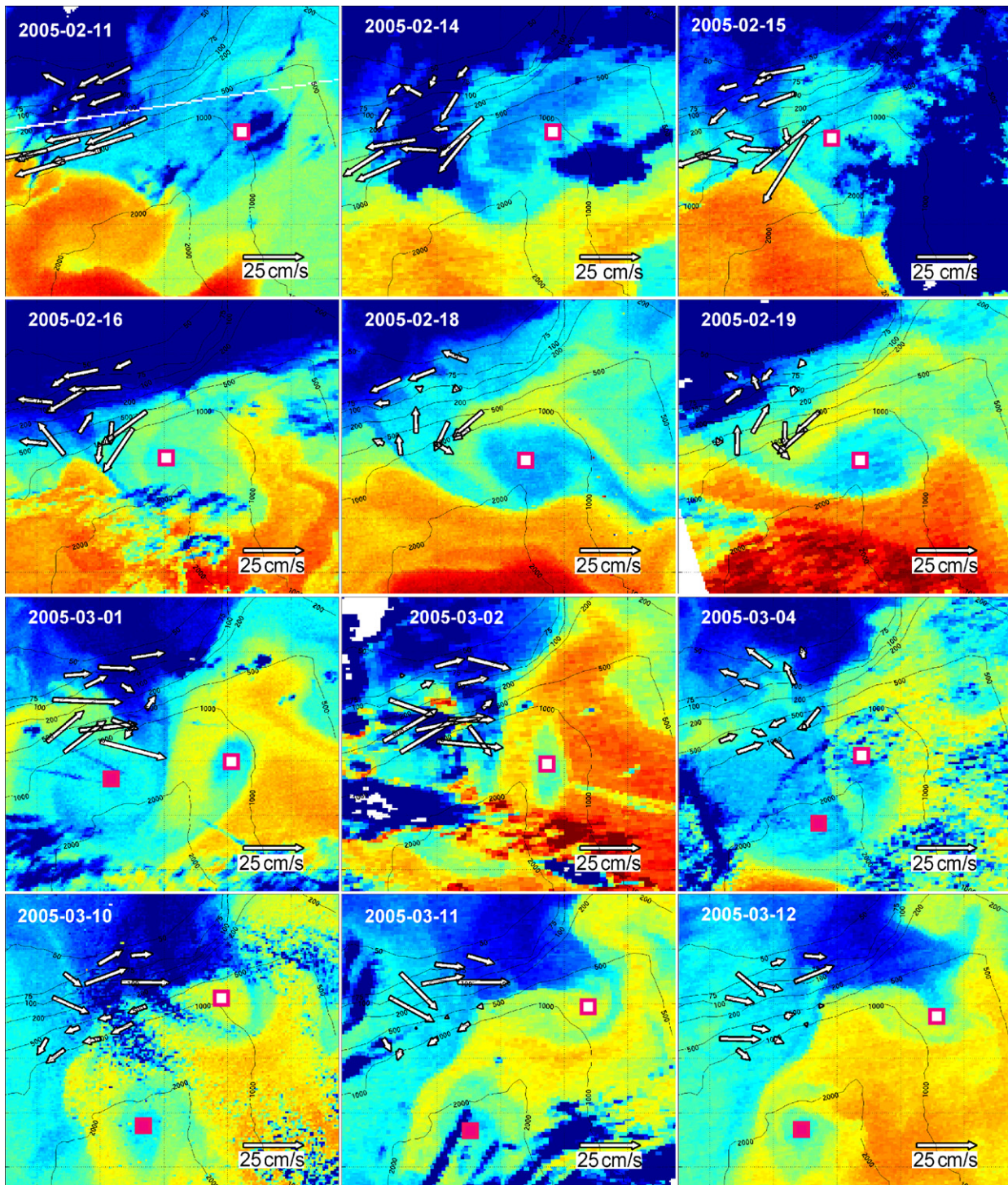


Fig. 15. MODIS color images of sea surface temperature at 1-km resolution showing the propagation and interaction of a cyclonic eddy (E2) and an anticyclonic eddy (E3) along the slope during D2. The temperature scale is the same for each plot and ranges from 17 °C (blue) to 25.5 °C (red). The red square with white center is the center of the cyclonic eddy (E2) and the red square is the center of the anticyclonic eddy (E3). Eddy E2 could not be located on day 2005-03-02 due to image noise. Vertically averaged currents are shown projecting from the mooring locations.

resulted in a reversal of the slope current and caused an upward arc in the slope mooring velocities (northeast on the western end and southeast on the eastern end). The cyclonic eddy (E2) center also moved eastward and was pinched inward in the east-west direction, apparently by the eastward encroachment by E3. Over the next 11 days,

E2 continued to move eastward, and E3 moved south southeast, and showed no obvious effect on the moorings after March 10.

Mode 2 EOF vectors (Fig. 10) and the associated amplitude time series (Fig. 11) of the D2 slope moorings appeared to be dominated by this two-eddy event. The

EOF vectors formed the north edge of side-by-side eddies, cyclonic E2 on the east and anticyclonic E3 on the west, with a southward jet near the middle. Mode 2 EOF amplitudes were small except from mid-February through the first week of March, when eddies were present and when large variations in the slope velocity (Fig. 13d) were not predicted well by wind stress. The average shelf velocity field during this time is predicted well from wind stress (Fig. 13b), indicating little influence by eddies.

During a 3-week period in March 2005 a strong eastward current developed along the slope with a maximum velocity near 0.2 m/s (Fig. 13d, bottom panel). There were no strong wind-related events that could explain this variation, as indicated by the small changes in the current predicted by the wind stress during this period. However, sea-surface-temperature and chlorophyll-concentration imagery were not found that could confirm that this variation in the slope current was associated with the impingement of an anticyclonic eddy. Sea surface height maps from satellite altimetry (Jacobs et al., 2002) indicate an anticyclonic eddy over the DeSoto Canyon that appears to impinge upon the moorings. However, the coarse space and time resolution of the altimetry cannot adequately resolve the small eddies observed in the imagery.

The northern edge of a cyclonic eddy (E4) was located over the slope moorings, causing westward flow during the

final month of D2. Fig. 16 shows a sequence of MODIS images from April 2, 2005 to April 16, 2005. The image on April 13 is of chlorophyll concentration and the other three images are of sea surface temperature. During this 2-week period, E4 remained nearly stationary with its center located over a bottom depth of about 2000 m. The radius, approximately 60 km, is about the same as E1. The average of the vertically averaged speeds in the upper 200 m over the slope moorings increased from a minimum of 0.082 m/s on April 4 to a maximum of 0.30 m/s on April 15 and then decreased to a minimum of 0.026 m/s on April 27. The last good image on April 16 is near the peak velocities. The maximum vertically averaged speed of 0.45 m/s occurred at mooring 11 (southwestern corner of array) on April 16. The moorings on the shelf exhibit a smaller westward velocity increase of about 0.10 m/s during the first half of the period when E4 influenced the slope mooring, starting on April 3, reaching a maximum on April 11, and ending on April 17.

9. Seasonal variability

Previous studies indicate that the flow on the north-eastern gulf slope is often dominated by the presence of cyclonic and anticyclonic eddies (Hamilton and Lee, 2005; Wang et al., 2003). However, during periods when eddies

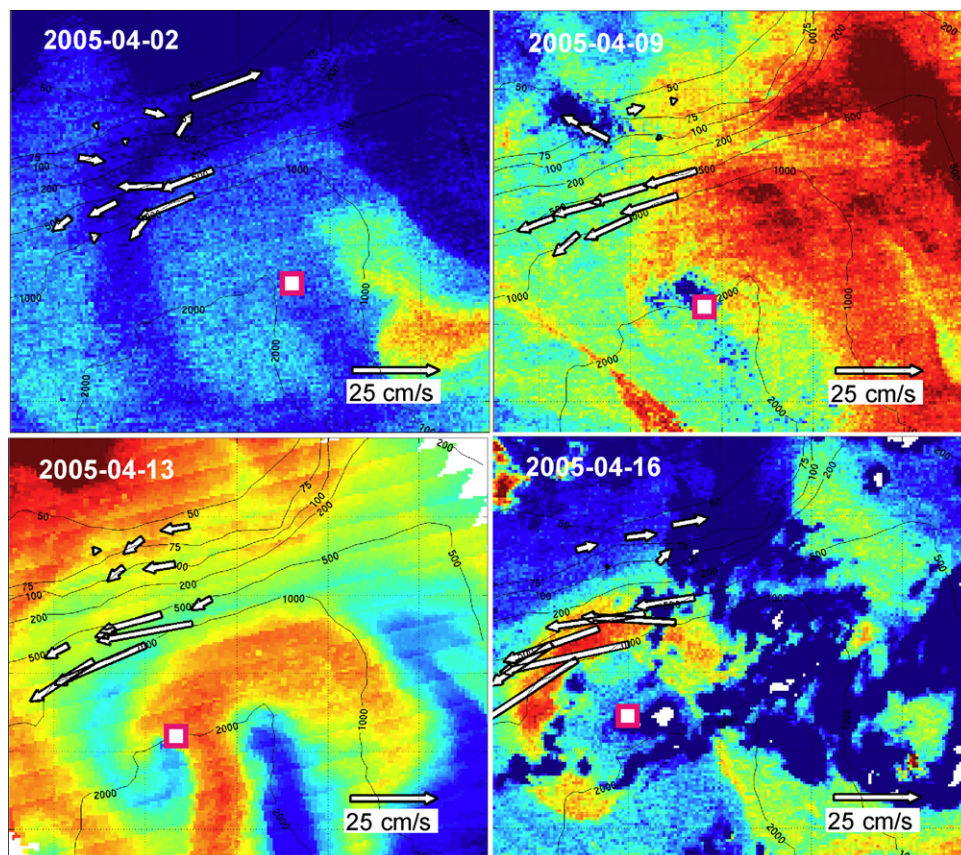


Fig. 16. MODIS color images of sea surface temperature (April 2, April 9, and April 16) and chlorophyll concentration (April 13), both at 1-km resolution showing the movement of E4 along the slope during D2. The temperature scale is the same for each plot and ranges from 17 °C (blue) to 25.5 °C (red). The red square with white center is the estimated center of the cyclonic eddy. Vertically averaged currents are shown projecting from the mooring locations.

were not observed near the slope moorings in 2004 and 2005, the difference between the observed vertically averaged along-shelf currents and those predicted from local wind stress (Fig. 13) exhibited long period trends, often near 0.2 m/s having a pronounced annual period and smaller semi-annual period signals (see Fig. 21 later in this section). Similar semi-annual variation in the along-shelf currents with approximately the same phase was also reported for this same region by Hsueh and Weisberg (2002) for the years 1997 and 1998. They computed monthly averages at 16-m depth using measurements made at four moorings from the DeSoto Canyon Eddy Intrusion Study (Hamilton et al., 2000) placed along the shelf break at 100 m depth from about 88.5°W (about 20 km west of the western side of the SEED mooring array) to 86.84°W (at the head of the DeSoto Canyon). At the two moorings bracketing the SEED mooring array, they found peak monthly mean eastward velocities centered in July (about 0.2–0.3 m/s) and December (near 0.2 m/s) and minimum eastward velocities in October and May (between 0 and 0.05 m/s). Using a high resolution Bryan-Cox model of the entire Gulf of Mexico, presented in Hsueh and Golubev (2002), they simulated the currents during the 1997–1998 period and presented plots of monthly averaged along-shelf currents at several depths over the slope near 88.5°W. Their results exhibited the same semi-annual variation as seen in the observations, with similar phase but with smaller amplitude. They argued that the semi-annual cycle of the slope current results from Ekman pumping due to the regional wind stress curl which also varies with a semi-annual cycle. They found that anticyclonic circulation, related to eastward velocity on the slope, reaches a peak about 1–1.5 months after the peak in negative wind stress curl. Furthermore, they show reasonable correspondence (presented for only one case) between modeled isotherm displacement and vertical displacement predicted from Ekman transport convergence due to wind stress curl.

A similar relationship was found by Flagg et al. (2006) between the seasonally varying slope current off the New Jersey coast and the regional wind stress curl. Furthermore, they found that the observed transport of the slope current matched the modeled transport utilizing Sverdrup balance by Csanady and Hamilton (1988) of the slope sea gyre.

In a small region where the change in the Coriolis parameter is small, the convergence of Ekman transport due to wind stress curl produces a vertical velocity at the base of the Ekman layer given by $w = -\nabla \times \bar{\tau} / \rho_0 f$. The isotherm displacement, h , as a function of time can be estimated by integrating the vertical velocity over time to obtain, $h(t) = h(0) - (1/\rho_0 f) \int_0^t \nabla \times \bar{\tau}(t') dt'$. In order to change the horizontal pressure gradient and change the geostrophic current below the Ekman layer, the wind stress curl must have a horizontal gradient (Yoshida, 1955). Two examples of the 1-month average wind stress curl and wind stress vectors over the Gulf of Mexico are shown in Fig. 17. The first, from June 2004, is from the time of year when average wind stress curl is most negative in the Gulf of Mexico, and the second, from February 2005, is from the period when it is least negative. Both were computed from the daily 27-km resolution Central America Coupled Ocean/Atmosphere Mesoscale Prediction System (COAMPS) surface wind vector grids. COAMPS is an atmospheric model and data assimilation system developed at the Naval Research Laboratory and run operationally at the Fleet Numerical Meteorology and Oceanography Center to provide nowcasts and forecasts (Hodur, 1997). These maps also illustrate the two dominate modes of wind stress in the Gulf of Mexico. During summer, the wind stress turns anticyclonically (strong negative curl) in response to the Bermuda High, but in winter, the wind forcing is dominated by the trade winds and passage of cold fronts (Molinari, 1987; Ford et al., 1988; Gutiérrez de Velasco and Winant, 1996). This seasonal change near the SEED moorings is shown in

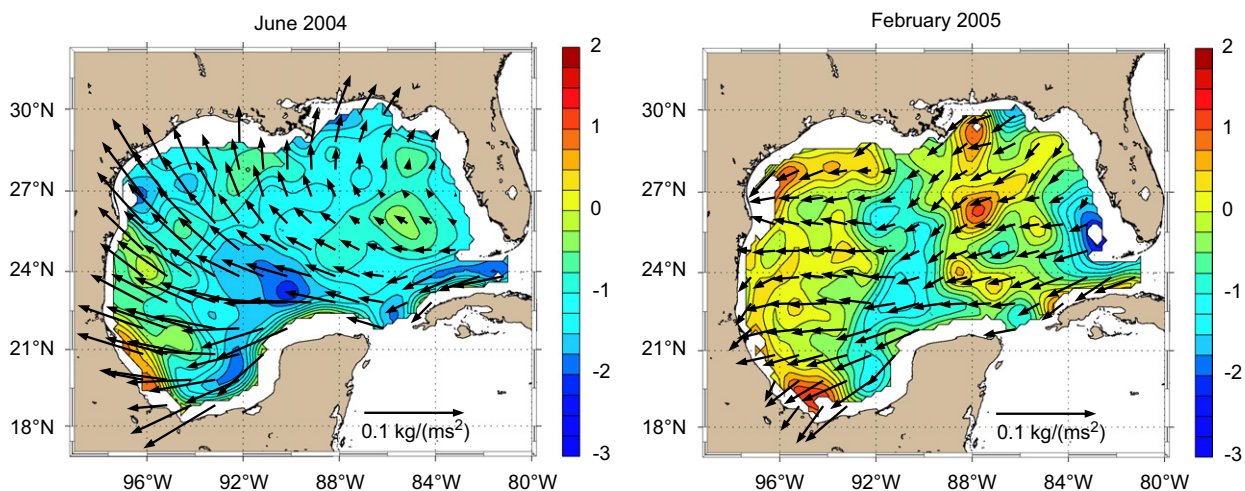


Fig. 17. Maps of 1-month averages of the wind stress vectors overlying color-filled contours of 1-month averages of the wind stress curl. Both were computed from daily COAMPS wind fields. Wind stress curl contours range from -3×10^{-7} to $2 \times 10^{-7} \text{ kg/m}^2 \text{ s}^2$ and the wind stress vector scale is shown in the lower right-hand corner.

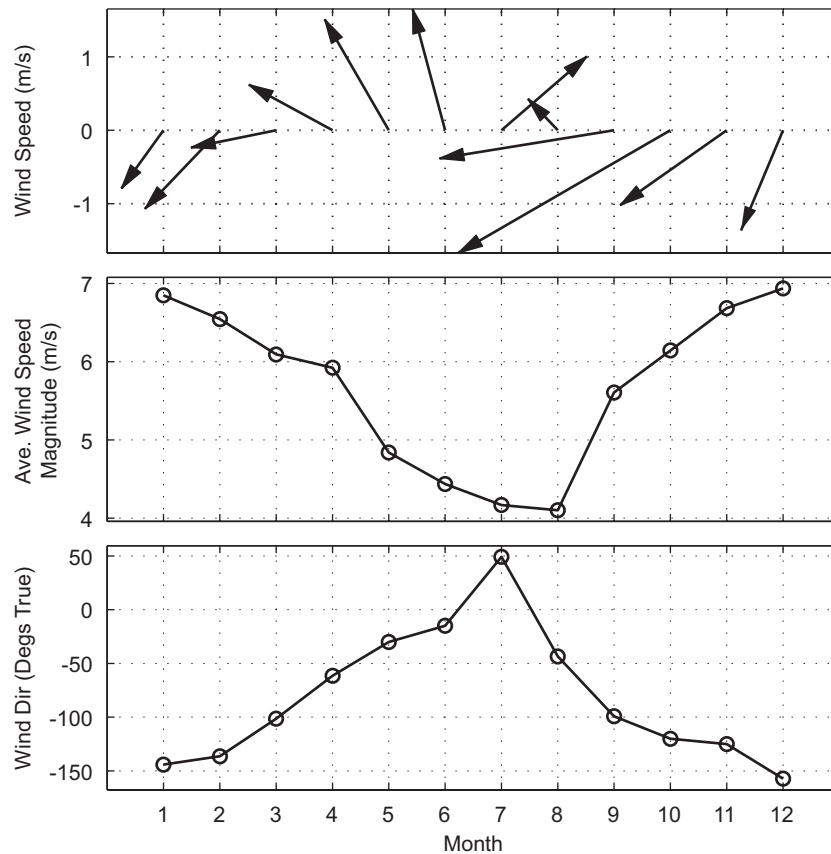


Fig. 18. Monthly averages of wind vectors, speed magnitude, and vector direction from measurements made at NOAA Buoy 42040 within the mooring array. Each monthly average was computed from measurements made over the 10-year period from 1996 to 2005.

Fig. 18 in the monthly average of vector winds, the magnitude of the wind speed, and the vector direction computed from wind observations made at NOAA Buoy 42040 (Fig. 1) over the 10-year period from 1996 to 2005. When the monthly average winds have a northward component, from April to August, the speed magnitudes are smallest (4–5 m/s) and during the rest of the year the speeds are mainly between 6 and 7 m/s.

The seasonal cycle in the winds is also evident in the wind stress curl, as shown in Fig. 19. This figure shows averages for each month for 2 years from January 2004 to December 2005 computed from the COAMPS wind fields. One curve is the curl averaged over the entire Gulf of Mexico west of 84°W , the second is the average over the northeast quadrant of the gulf (90°W – 84°W and 24°N – 31°N), and the third is the average over the region near the SEED moorings (90 – 86.5°W and 27.5°N – 29.5°N). Also shown is the two-year mean of each curve. The curves of monthly averages of curl for the entire Gulf of Mexico used here are similar to eastern gulf and western gulf wind stress curl multi-year monthly averages used by Oey (1995) which he computed from European Centre for Medium-Range Weather Forecasts (ECMWF) winds. The annual means are similar, but the two distinct cycles per year are more prominent in the smaller region averages used here than in the full-gulf averages. The single-month averages

for the smaller areas have large rapid changes due, in some cases, to individual storms, particularly hurricanes during the summer. However, the full-gulf wind-stress curl averages have largest magnitudes (negative and below the mean) during the period when the winds (Fig. 18) are weakest and toward the north, while they have lowest magnitudes when winds are strongest and from the northeast. The full-gulf averages (Fig. 19) show one cycle per year, but flatten out between September and May. The average from the two smaller regions are very similar and have a semi-annual variation, but with large differences between the 2 years.

As discussed above, a simple dynamical model of Ekman pumping indicates that geostrophic current velocities should be proportional to the time integral of the wind stress curl. Since the integrated wind stress curl provides a prediction of the currents, the integral from the most effective generation region should be most similar to the seasonal variation of the measured currents. The integrated wind stress curl averaged over each of the regions discussed above is shown in Fig. 20 for the full gulf, the northeast quadrant of the gulf, and the region near the SEED moorings. For each case, the 2-year mean was removed before integrating and then the mean of the integrated result was removed. In addition, the integrals were multiplied by -1 so that anticyclonic (negative) curl integrals

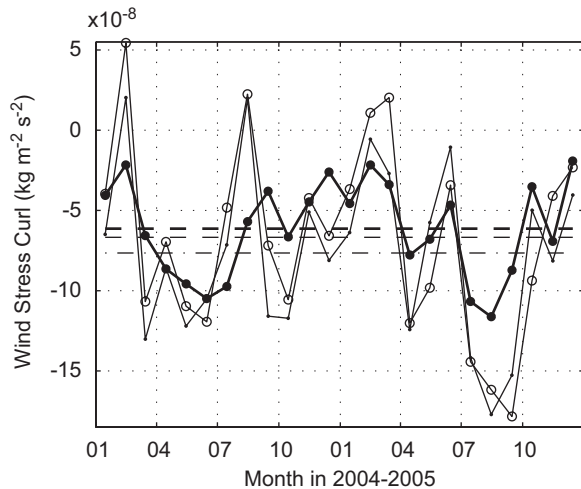


Fig. 19. Area averages of monthly averages of wind stress curl for years 2004 and 2005. Monthly averages were from daily grids of curl computed from the $1/5^\circ$ -resolution COAMPS wind stress grids. The thick line is an average over the full Gulf of Mexico, the thin line with small dot markers is average over the northeast quadrant of the Gulf of Mexico ($90\text{--}84^\circ\text{W}$ and $25.5\text{--}31^\circ\text{N}$), and the thin line with open circle markers is the region close to the SEED moorings ($90\text{--}86.5^\circ\text{W}$ and $27.5\text{--}29.5^\circ\text{N}$). Values are plotted at the center of each month. Horizontal lines are 2-year wind stress curl averages for the full gulf (thick dashed, $-6.1 \times 10^{-8} \text{ kg/m}^2 \text{ s}^2$), the northeast quadrant of the gulf (thin line dash dot, $-7.7 \times 10^{-8} \text{ kg/m}^2 \text{ s}^2$), and the region near the SEED moorings (thin dashed, $-6.7 \times 10^{-8} \text{ kg/m}^2 \text{ s}^2$). Daily wind stress curl values were included in averages only when the absolute value was less than $5 \times 10^{-7} \text{ kg/m}^2 \text{ s}^2$ and only where water depth is greater than 30 m.

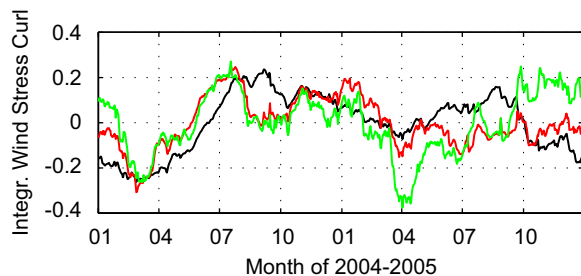


Fig. 20. Time series of the detrended time integral of the negative wind stress curl ($\text{kg/m}^2 \text{ s}$) over different block areas in the Gulf of Mexico (GOM). Line colors and geographic areas are: Black: Full GOM west of 84°W ; Red: Northeast quadrant ($90\text{--}84^\circ\text{W}$, north of 25.5°N), Green: Area near SEED moorings ($90\text{--}86.5^\circ\text{W}$ and $27.5\text{--}29.5^\circ\text{N}$).

align with eastward (positive) velocities along the northern gulf. If the mean of the curl had not been removed before integrating, an additional linear trend spanning about $4 \text{ kg/m}^2 \text{ s}$ would have been added to the integrated curves, about 10 times the variation of the detrended results. The curves are noisy because each value is an average in only 1 year. They show minima in March–April and maxima in late summer to early fall.

Oey (1995) studied the full Gulf of Mexico circulation using a model forced by wind stress curl but without flow through the Yucatan and Florida Straits and found that the currents in the northeastern gulf appeared to be an

extension of the slope currents south of the Texas–Louisiana shelf but lagged the peaks in wind stress curl by a few months. The integrated wind stress curl averaged over the full gulf (Fig. 20) provides the best match to the observed currents and is compared to the vertically averaged currents in Fig. 21. The observed currents in this figure are averages of the along-shelf component of velocity over all ADCP measurements made at the slope moorings (bottom depths of moorings at 500 and 1000 m) averaged over the upper 200 m during D1 and D2. The full-gulf time series of integrated wind stress curl (from Fig. 20) was approximately matched to the observations by multiplying by $1.4 \text{ m}^3/\text{kg}$, but with no offset applied. In addition, the detrended time-integral of the component of wind stress toward 135°T (divided by 35,000 for matching purposes) from the nearby NOAA Buoy 42040 is also plotted in Fig. 21. Remarkably, the wind stress integral and the wind stress curl integral curves match well, and both are similar to the observed along-shelf velocity. The symbols E1–E4 mark the times when cyclonic and anticyclone eddies were impinging on the slope moorings, and the W symbol marks two points where large velocity fluctuations were predicted accurately from wind stress (see Fig. 13d, upper frame). Other than these two wind-related events and the times when eddies were present, the largest discrepancy with the two integral curves in Fig. 21 occurred in September when the observed current decreased from 0.25 m/s to near zero while the curl integral decreased more slowly. Data were not available from the NOAA Buoy for a period after the passage of Hurricane Ivan. The wind stress integral was carried forward during this time period by setting wind stress to 0. During this anomalous period, i.e., during and after Hurricane Ivan, the curl integrals from the local area are more similar to the observed currents than the curl integral for the entire gulf, but the downturn in current velocity after its peak occurs earlier than the downturn in the curl for the entire gulf but later than the downturns for the local areas (see Fig. 20). In many ways,

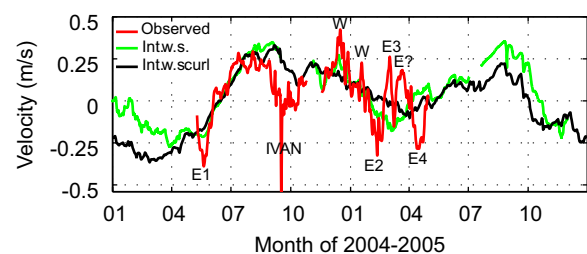


Fig. 21. Red: Time series of vertically averaged (in upper 200 m) observed along-shelf current averaged over all slope moorings (M7–M14 during D1 and M7–M13 during D2). Green: Detrended time integral of wind stress component along 135°T measured at NOAA Buoy 42040 divided by 35,000. Black: Detrended time integral of wind stress curl multiplied by (-1.4) averaged over the Gulf of Mexico east of 84°W . The symbols E1–E4 mark the times when eddies were observed in MODIS imagery to be impinging on the slope moorings. The symbol W marks times when large fluctuations in the current were predicted well by a simple vertically integrated Ekman model.

the observations appear to match an average of the three curl integral curves better than any single curve. Due to the over-simplified nature of the dynamics of the expected relationship between along-shelf slope currents and the integrated wind stress curl, we should expect only general agreement. However, the close agreement between the unlagged SEED currents with the integrated wind stress curl is remarkable. Note that the integrated wind stress for the local region matched the integrated wind stress curl for the entire region, which was found not to be the case when wind stress time series from other areas in the gulf were used. This perhaps fortuitous matching deserves further study.

10. Summary and conclusions

We have shown that the low-frequency flows are mainly driven by wind and eddies and that the dominant flow pattern is along-shelf or along bathymetry. Currents were modulated on time scales that ranged from a couple of days to about a week on the shelf and from 1 to 2 weeks on the slope, with the longer time scales occurring in the along shelf direction. Barotropic processes accounted for about 80% of the energy. The maximum observed speeds exceeded 60 cm/s but since the flow commonly reversed direction, the average current speeds were generally much less than 10 cm/s. By dividing the D2 time period into four periods, some significant mean flow directions were found. The resultant flow for the winter–spring period was offshore and upcoast for all of the shelf moorings, except for M6 where the flow was primarily upcoast. The resultant flow on the slope was generally upcoast and onshore on the western half of L3 and downcoast and offshore on the eastern half of L3, and generally upcoast on L4 with an onshore component on the western end and an offshore component on the eastern end of L4. At least four mesoscale eddies were identified that affected the SEED region currents. One eddy occurred at the beginning of the D1 while the other three occurred during D2. The maximum correlation of the currents with the wind stress occurred at a wind direction of about 150°T, which is the general direction of the West Florida shelf and implies that the currents in the SEED region may be driven by processes such as shelf waves, for example, generated by wind forcing along the west Florida shelf.

The first 2 EOFs accounted for 72% and 87% of the along-shelf velocity variance but only for 7% and 22% of the cross-shelf velocity variance, for the shelf and slope, respectively. Cross-shelf variability was also poorly correlated between the individual moorings and was affected by eddy intrusions. The first EOF was dominated by the along-shelf flows driven by the winds and eddies. The second EOF on the slope was dominated by the pair of eddies in March that caused significant onshore and offshore flows. The other eddies mainly affected the along-shelf flows and did not have a signature in the second EOF on the slope.

Although it is known that the circulation could be driven by the curl of the wind stress and eddy interactions, their relative importance to the background seasonal circulation patterns has not previously been well determined. Previous studies have shown that the wind stress curl is important as a driving mechanism for the currents in the western and eastern Gulf of Mexico. It was not clear on what scale, basin or sub-basin, the wind stress is most effective. Generally, a time lag was found between the currents and wind stress curl. Here, we have presented evidence that circulation is affected by the winds on a variety of spatial and temporal scales. Wind stress at the surface balanced by bottom friction controls shelf and slope currents with time scales on the order of a week or two. There is also a clear seasonal pattern in the currents that is related to the winds. The general upcoast and downcoast background circulation is driven by the winds throughout the year. These currents are highly correlated with the integrated wind stress curls on the basin and sub-basin scales and contain similarities to basic features of the wind stress on each scale. There is effectively no lag between the currents and integrated wind stress curl. Therefore, use of integrated wind stress curl instead of wind stress removes the lag. Here we show that larger current accelerations occurred during the periods of larger wind stress curl which occurred during periods of weaker summer winds. Our analyses show that eddies can significantly alter the flow patterns on the shelf and slope, and even reverse the direction of the currents. Spikes in the local wind stress can cause effects similar to those caused by eddies in the background flow.

Eddies and storm events, such as hurricanes, have been thought to be major contributors to cross-shelf exchange. The effect of Hurricane Ivan during D1 was short term and was minor in the cross-shelf exchange (Teague et al., 2006). Eddy intrusions were smaller in number during D1 than during D2. During D2, at least three eddies had an impact on the exchange and contributed significantly to the onshore and offshore exchange on the slope (L3 and L4) and on the 90 m mooring line (L2). The ranges of the cross-shelf exchange expressed by CVT (Fig. 6) during D2 were similar to those in D1 along the slope but were about twice as large as those in D1 on the shelf. Hence, other processes must also be important in the cross-shelf exchange, such as those related to winds, pressure gradients, and non-local forcing events.

Acknowledgments

This work was supported by the Office of Naval Research as part of the Naval Research Laboratory's basic research project "Slope to Shelf Energetics and Exchange Dynamics (SEED)" under program element 0601153N (NRL-SSC contribution NRL/JA/7330—05-5172). Two anonymous reviewers provided valuable suggestions for improving the manuscript.

References

- Beardsley, R.C., Chapman, D.C., Brink, K.H., Ramp, S.R., Schlitz, R., 1985. The Nantucket Shoals Flux Experiment (NSFE79): I. A basic description of the current and temperature variability. *Journal of Physical Oceanography* 15, 713–748.
- Biggs, D.C., Jochens, A. E., Howard, M.K., DiMarco, S.F., Mullin, K.D., Leben, R.R., Muller-Karger, F.E., Hu, C., 2005. Eddy forced variations in on- and off-margin summertime circulation along the 1000-m isobath of the northern Gulf of Mexico, 2000–2003, and links with sperm whale distributions along the middle slope. In: Wilton Sturges, Alexis Lugo-Fernandez (Eds.), *Circulation in the Gulf of Mexico: Observations and Models*, Geophysical Monograph Series 161, pp. 71–86, [10.1029/161GM06](#).
- Blaha, J., Sturges, W., 1981. Evidence for wind-forced circulation in the Gulf of Mexico. *Journal of Marine Research* 39 (4), 711–734.
- Chassignet, E.P., Hurlburt, H.E., Smedstad, O.M., Halliwell, G.R., Hogan, P.J., Wallcraft, A.J., Baraille, R., Bleck, R., 2007. The HYCOM (HYbrid Coordinate Ocean Model) data assimilative system. *Journal of Marine Systems* 65, 60–83.
- Csanady, G.T., 1974. Barotropic currents over the continental shelf. *Journal of Physical Oceanography* 4, 357–371.
- Csanady, G.T., Hamilton, P., 1988. Circulation of slope water. *Continental Shelf Research* 8, 565–624.
- Flagg, C.N., Dunn, M., Wang, D.-P., Rossby, H.T., Benway, R.L., 2006. A study of the currents of the outer shelf and upper slope from a decade of shipboard ADCP observations in the Middle Atlantic Bight. *Journal of Geophysical Research* 111, C06003.
- Ford, J., Wayland, R., Waddell, E., Hamilton, B., 1988. Meteorological Database and Synthesis for the Gulf of Mexico, OCS Study, MMS 88-0064. US Dept. of the Interior, Mineral Management Service, New Orleans, LA, 486pp.
- Gutiérrez de Velasco, G., Winant, C.D., 1996. Seasonal patterns of wind stress and wind stress curl over the Gulf of Mexico. *Journal of Geophysical Research* 101, 18127–18140.
- Hallock, Z.R., Teague, W.J., Jarosz, E., submitted. Topographic Rossby waves on the slope in the northeastern Gulf of Mexico. *Journal of Physical Oceanography*.
- Hamilton, P., Lee, T.N., 2005. Eddies and jets over the slope of the northeast Gulf of Mexico. In: Sturges, W., Lugo-Fernandez, A. (Eds.), *Circulation in the Gulf of Mexico: Observations and Models*, Geophysical Monograph Series 161, pp. 123–142, [10.1029/161GM10](#).
- Hamilton, P., Berger, T.J., Singer, J.J., Waddell, E., Churchill, J.H., Leben, R.R., Lee, T.N., Sturges, W., 2000. Desoto Canyon Eddy Intrusion Study, Final Report, vol. II: Technical Report, OSC Study MMS 2000-080. US Department of the Interior, Mineral Management Service, Gulf of Mexico OCS Region, New Orleans, LA, 275pp.
- Hickey, G.M., Dobbins, E.L., Allen, S.E., 2003. Local and remote forcing of currents and temperature in the central Southern California Bight. *Journal of Geophysical Research* 108 (C3), 3081.
- Hodur, R.M., 1997. The Naval Research Laboratory's Coupled Ocean/Atmosphere Mesoscale Prediction System (COAMPS). *Monthly Weather Review* 125, 1414–1430.
- Hsueh, Y., Golubev, Y., 2002. A numerical model calculation of the flow in DeSoto Canyon in response to northerly wind bursts in winter. *Gulf of Mexico Science* 20, 44–59.
- Hsueh, Y., Weisberg, R., 2002. Northeastern Gulf of Mexico Circulation Modeling Study: Final Report, MMS Cooperative agreement 14-35-0001-30804. OCS Study MMS 2002-053. US Department of the Interior, Minerals Management Service, Herndon, VA, 187pp. (Note: handles Golubev and Hsueh.)
- Huh, O.K., Wiseman Jr., W.J., Rouse Jr., L.J., 1981. Intrusion of Loop Current Waters onto the West Florida Continental Shelf. *Journal of Geophysical Research* 86, 4186–4192.
- Jacobs, G.A., Barron, C.N., Fox, D.N., Whitmer, K.R., Klingenberg, S., May, D., Blaha, J.P., 2002. Operational altimeter sea level products. *Oceanography* 15, 13–21.
- Jarosz, E., Murray, S.P., 2005. Velocity and transport characteristics of the Louisiana–Texas coastal current. In: Sturges, W., Lugo-Fernandez, A. (Eds.), *Circulation in the Gulf of Mexico: Observations and Models*, Geophysical Monograph Series 161, pp. 143–156, [10.1029/161GM11](#).
- Johnson, W., 2005. Movies of surface drifters in the northern Gulf of Mexico. In: Sturges, W., Lugo-Fernandez, A. (Eds.), *Circulation in the Gulf of Mexico: Observations and Models*, Geophysical Monograph Series 161, p. 157, [10.1029/161GM12](#).
- Lentz, S., Winant, C.D., 1986. Subinertial currents on the South California shelf. *Journal of Physical Oceanography* 16, 1737–1750.
- Li, Z., Weisberg, R.H., 1999. West Florida shelf response to upwelling favorable wind forcing: kinematics. *Journal of Geophysical Research* 104, 13507–13527.
- Liu, Y., Weisberg, R.H., 2007. Ocean currents and sea surface heights estimated across the West Florida Shelf. *Journal of Physical Oceanography* 37, 1697–1713.
- Maul, G.A., Vukovich, F.M., 1993. The relationship between variations in the Gulf of Mexico Loop Current and Straits of Florida volume transport. *Journal of Physical Oceanography* 23, 785–796.
- Mendoza, V.M., Villanueva, E.E., Adem, J., 2005. On the annual cycle of the sea surface temperature and the mixed layer depth in the Gulf of Mexico. *Atmosfera* 18 (2), 127–148.
- Molinari, R.L., 1987. Air mass modification over the eastern Gulf of Mexico as a function of surface wind fields and loop current position. *Monthly Weather Review* 115, 646–652.
- Morey, S.L., Zavala-Hidalgo, J., O'Brien, J.J., 2005. The seasonal variability of continental shelf circulation in the northern and western Gulf of Mexico from a high-resolution numerical model. In: Sturges, W., Lugo-Fernandez, A. (Eds.), *Circulation in the Gulf of Mexico: Observations and Models*, Geophysical Monograph Series 161, pp. 203–218, [10.1029/161GM16](#).
- Oey, L.-Y., 1995. Eddy- and wind-forced shelf circulation. *Journal of Geophysical Research* 100, 8621–8637.
- Overland, J.E., Preisendorfer, R.W., 1982. A significance test for principal components applied to a cyclone climatology. *Monthly Weather Review* 110, 1–4.
- Perkins, H., De Strobel, F., Gauldesi, L., 2000. The barny sentinel trawl-resistant ADCP bottom mount: design, testing, and application. *IEEE Journal of Oceanic Engineering* 25, 430–436.
- Preisendorfer, R.W., 1988. *Principal Component Analysis in Meteorology and Oceanography*. Elsevier, Amsterdam, (425pp.).
- Shearman, R.K., Lentz, S.J., 2003. Dynamics of mean and subtidal flow on the New England shelf. *Journal of Geophysical Research* 108 (C8), 3281.
- Sturges, W., 1992. An estimate of the spectrum of Loop Current variability from gappy data. *Journal of Physical Oceanography* 22, 1245–1256.
- Sturges, W., 1993. The annual cycle of the Western Boundary Current in the Gulf of Mexico. *Journal of Geophysical Research* 98, 18053–18068.
- Sturges, W., Blaha, J.P., 1976. A western boundary current in the Gulf of Mexico. *Science* 192, 367–369.
- Teague, W.J., Jarosz, E., Carnes, M.R., Mitchell, D.A., Hogan, P.J., 2006. Low-frequency current variability observed at the shelfbreak in the northeastern Gulf of Mexico: May–October 2004. *Continental Shelf Research* 26, 2559–2582.
- Teague, W.J., Jarosz, E., Wang, D.W., Mitchell, D.A., 2007. Observed oceanic response over the upper continental slope and outer shelf during Hurricane Ivan. *Journal of Physical Oceanography* 37 (9), 2181–2206.
- Vukovich, F.M., 1988. Loop Current boundary variations. *Journal of Geophysical Research* 93, 15585–15591.
- Vukovich, F.M., Maul, G.A., 1985. Cyclonic eddies in the eastern Gulf of Mexico. *Journal of Physical Oceanography* 15, 105–117.
- Vukovich, F.M., Crissman, B.W., Bushnell, M., King, W.J., 1979. Some aspects of the oceanography of the Gulf of Mexico using satellite and in-situ data. *Journal of Geophysical Research* 84, 7749–7768.

- Wang, D., Oey, L., Ezer, T., Hamilton, P., 2003. Near-surface currents in DeSoto Canyon (1997–99): comparison of current meters, satellite observation, and model simulation. *Journal of Physical Oceanography* 33, 313–326.
- Weisberg, R.H., He, R., Liu, Y., Virmani, J.I., 2005. West Florida shelf circulation on synoptic, seasonal, and interannual time scales. In: Sturges, W., Lugo-Fernandez, A. (Eds.), *Circulation in the Gulf of Mexico: Observations and Models*, Geophysical Monograph Series 161, pp. 325–347, [10.1029/161GM23](https://doi.org/10.1029/161GM23).
- Wiseman Jr., W.J., Dinnel, S.P., 1988. Shelf currents near the mouth of the Mississippi River. *Journal of Physical Oceanography* 18, 1287–1291.
- Yoshida, K., 1955. An example of variations in oceanic circulation in response to variations in the wind field. *Journal of Oceanographical Society of Japan* 11, 103–108.
- Yuan, D., 2002. A numerical study of barotropically forced intrusion in DeSoto Canyon. *Journal of Geophysical Research* 107 (C2), 3010.